



Published in final edited form as:

Cell Rep. 2021 July 20; 36(3): 109422. doi:10.1016/j.celrep.2021.109422.

Immune mechanisms orchestrate tertiary lymphoid structures in tumors via cancer-associated fibroblasts

Anthony B. Rodriguez^{1,2}, J. David Peske^{1,2,6}, Amber N. Woods^{1,2}, Katie M. Leick^{1,3}, Ileana S. Mauldin^{1,3}, Max O. Meneveau³, Samuel J. Young^{1,3}, Robin S. Lindsay^{1,2}, Marit M. Melssen^{1,3}, Salvador Cyranowski¹, Geoffrey Parriott¹, Mark R. Conaway⁴, Yang-Xin Fu⁵, Craig L. Slingluff Jr.^{1,3}, Victor H. Engelhard^{1,2,7,*}

¹Beirne B. Carter Center for Immunology Research, University of Virginia School of Medicine, Charlottesville, VA 22908, USA

²Department of Microbiology, Immunology and Cancer Biology, University of Virginia School of Medicine, Charlottesville, VA 22908, USA

³Department of Surgery, University of Virginia School of Medicine, Charlottesville, VA 22908, USA

⁴Division of Translational Research & Applied Statistics, Department of Public Health Sciences, University of Virginia School of Medicine, Charlottesville, VA 22908, USA

⁵Department of Pathology, University of Texas Southwestern Medical Center, Dallas, TX 75235, USA

⁶Present address: Department of Pathology, Johns Hopkins University, Baltimore, MD 21218, USA

⁷Lead contact

SUMMARY

Tumor-associated tertiary lymphoid structures (TA-TLS) are associated with enhanced patient survival and responsiveness to cancer therapies, but the mechanisms underlying their development are unknown. We show here that TA-TLS development in murine melanoma is orchestrated by cancer-associated fibroblasts (CAF) with characteristics of lymphoid tissue organizer cells that are induced by tumor necrosis factor receptor signaling. CAF organization into reticular networks is mediated by CD8 T cells, while CAF accumulation and TA-TLS expansion depend on CXCL13-mediated recruitment of B cells expressing lymphotoxin- $\alpha_1\beta_2$. Some of these elements are also overrepresented in human TA-TLS. Additionally, we demonstrate that immunotherapy induces more and larger TA-TLS that are more often organized with discrete T and B cell zones, and that

This is an open access article under the CC BY-NC-ND license (<http://creativecommons.org/licenses/by-nc-nd/4.0/>).

*Correspondence: vhe@virginia.edu.

AUTHOR CONTRIBUTIONS

Murine experiments were performed and analyzed by A.B.R., J.D.P., A.N.W., K.M.L., M.M.M., R.S.L., S.C., and G.P. Murine IF analysis was performed by R.S.L. Multispectral imaging was performed and analyzed by K.M.L., I.S.M., S.J.Y., and A.B.R. Statistical analysis of human multispectral imaging data was done by M.O.M. and M.R.C. V.H.E. and C.L.S. supervised experimental design and data interpretation. All authors contributed to manuscript preparation.

DECLARATION OF INTERESTS

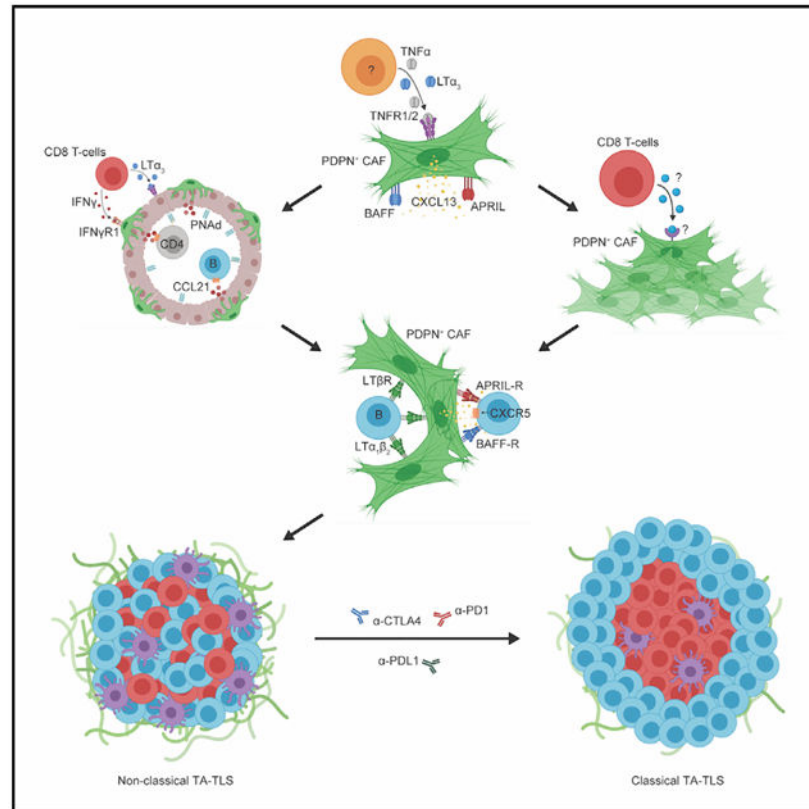
The authors declare no competing interests.

SUPPLEMENTAL INFORMATION

Supplemental information can be found online at <https://doi.org/10.1016/j.celrep.2021.109422>.

TA-TLS presence, number, and size are correlated with reduced tumor size and overall response to checkpoint immunotherapy. This work provides a platform for manipulating TA-TLS development as a cancer immunotherapy strategy.

Graphical Abstract



In brief

Rodriguez et al. describe the cellular and molecular mechanisms driving development of tumor-associated tertiary lymphoid structures and the importance of these structures as mediators of anti-tumor immunity and response to checkpoint immunotherapy.

INTRODUCTION

Tertiary lymphoid structures (TLS) are ectopic aggregates with morphological, cellular, and molecular similarities to secondary lymphoid organs (SLO) and commonly found with chronic infection, autoimmunity, and organ transplantation (Neyt et al., 2012; Koenig and Thauat, 2016). TLS are found in human tumors (tumor-associated TLS [TA-TLS]) and are usually associated with higher representations of tumor-infiltrating lymphocytes (TIL), enhanced patient survival, and clinical responses to chemotherapy and immunotherapies (Engelhard et al., 2018; Sautès-Fridman et al., 2019; Rodriguez and Engelhard, 2020). It has been suggested that TA-TLS are sites for sustained antitumor immunity, and that

TA-TLS augmentation could be a new strategy for cancer immunotherapy. This depends on understanding the mechanisms driving TA-TLS development.

Mechanisms governing development of SLOs are well established (reviewed in van de Pavert and Mebius, 2010; Onder and Ludewig, 2018; Mueller et al., 2018). SLO development depends on interaction between innate lymphoid type 3 (ILC3) lymphoid tissue inducer (LTi) cells expressing surface lymphotoxin- $\alpha_1\beta_2$ (LT $\alpha_1\beta_2$) and mesenchymal lymphoid tissue organizer (LTo) cells expressing lymphotoxin- β receptor (LT β R). LTo cells mature into CXCL13-producing follicular dendritic cells (FDC) and CCL19/21-producing fibroblastic reticular cells (FRC), which facilitate recruitment and compartmentalization of T and B cells. Although some chronic inflammation-associated TLS also depend on LT β R signaling (Furtado et al., 2007; Gatumu et al., 2009; GeurtsvanKessel et al., 2009; Gräbner et al., 2009; Motallebzadeh et al., 2012; Pikor et al., 2015), others depend on IL-5, IL-6, IL-17, IL-22, IL-23, and/or TNF- α , either in conjunction with (Lötzer et al., 2010; Rangel-Moreno et al., 2011; Pikor et al., 2015) or independent of (Lee et al., 1997; Goya et al., 2003; Khader et al., 2011; Peters et al., 2011; Furtado et al., 2014; Guedj et al., 2014; Barone et al., 2015; Bénézéch et al., 2015; Cañete et al., 2015) LT β R signaling. CCL19, CCL21, CXCL12, and CXCL13 are found in TLS (Rangel-Moreno et al., 2007; Fleige et al., 2014; Barone et al., 2015; Sato et al., 2016), along with cells expressing FRC (Peduto et al., 2009; Link et al., 2011) or FDC (Drayton et al., 2003; Bombardieri et al., 2007) surface markers, and some of the inflammatory cytokines identified above can upregulate chemokine expression in cultured smooth muscle cells (Lötzer et al., 2010; Guedj et al., 2014) and fibroblasts purified from inflamed tissues containing TLSs (Khader et al., 2011; Rangel-Moreno et al., 2011; Barone et al., 2015). However, only one report has directly demonstrated that LTo-like fibroblasts could support TLS development (Nayar et al., 2019). Inflammatory TLS development can also depend on a variety of LTi cells, including dendritic cells (DC) (GeurtsvanKessel et al., 2009; Halle et al., 2009; Muniz et al., 2011), B cells (McDonald et al., 2005; Dubey et al., 2016), macrophages (Furtado et al., 2014; Guedj et al., 2014; Bénézéch et al., 2015), T_H17 cells (Peters et al., 2011; Rangel-Moreno et al., 2011; Pikor et al., 2015), natural killer T (NKT) cells (Bénézéch et al., 2015), $\gamma\delta$ T cells (Fleige et al., 2014), and multiple populations of IL-22-secreting adaptive and innate lymphoid cells (Barone et al., 2015). The heterogeneous drivers of TLS development likely depend on microenvironmental context. However, the cellular and molecular drivers of TA-TLS are undefined.

Vaccination can induce TA-TLS development in pancreatic tumors (Lutz et al., 2014) and cervical neoplastic lesions (Maldonado et al., 2014). TA-TLS development in murine tumors has been induced by transgenic overexpression of LT β R ligands (Schrama et al., 2001; Kim et al., 2004; Yu et al., 2004, 2007), injection of recombinant LIGHT (Johansson-Percival et al., 2017), and intratumoral administration of CCL21 (Kirk et al., 2001; Turnquist et al., 2007). However, there are few reports of spontaneous TA-TLS development in murine tumors (Finkin et al., 2015; Joshi et al., 2015; Peske et al., 2015; Rodriguez et al., 2018). We previously demonstrated that naive T cells infiltrated murine tumors, underwent *in situ* activation, and augmented tumor control (Thompson et al., 2010; Peske et al., 2015). Naive T cell entry depended on tumor endothelial cells expressing peripheral node addressin (PNAd) and CCL21, which in turn depended on effector CD8 T cells and

natural killer (NK) cells secreting $LT\alpha_3$ and $IFN-\gamma$ (Peske et al., 2015). We subsequently showed that tumors growing in the peritoneal cavity (intraperitoneally [I.P.]), but not those growing subcutaneously (S.C.), had TA-TLS adjacent to $PNAd^+$ vasculature (Peske et al., 2015; Rodriguez et al., 2018). Here, we identify the cellular and molecular mechanisms driving TA-TLS development. Our results highlight the pivotal role of cancer-associated fibroblasts (CAF) as surrogate $LT\alpha$ cells and highlight multiple cell types, including intratumoral CD8 T cells and $LT\alpha_1\beta_2^+$ B cells, that synergistically act as LTi cells. They also demonstrate that TA-TLS development and organization are augmented by checkpoint blockade immunotherapy and are associated with reduced tumor size.

RESULTS

TA-TLS in I.P. tumors are associated with altered distributions of activated T cells and naïve B cells

By seven-color immunofluorescence (IF), we observed dense multicellular structures adjacent to $PNAd^+$ vessels in I.P. B16-OVA tumors (Figure 1A; Figures S1A–S1C). However, these structures never formed in S.C. tumors. TA-TLS were dominated by a dense aggregate of B cells. In most cases, CD4 T cells were scattered throughout the B cell aggregate, while CD8 T cells and DCs were found predominantly on the periphery and also were not well organized (Figures S1D–S1G). These structures resemble “non-classical” TA-TLS seen in murine and human hepatocellular carcinoma (Finkin et al., 2015). I.P. tumors also contained less frequent “classical” TA-TLS with distinct T and B cell compartments (Figure 1A). TA-TLS were also present in parental B16-F1 I.P. tumors, although they were smaller and fewer (Figures S1H and S1I). TA-TLS were also present in B16-OVA tumors grown in lung and in I.P., but not S.C., MC38 and LLC tumors (Figures S1J–S1L). Thus, TA-TLS quantity and quality are associated with antigen strength, but their presence is due to tumor microenvironmental factors that depend on anatomical location.

I.P. B16 tumors grow as single pigmented masses, not ascites, juxtaposed to stomach, cecum, spleen, pancreas, and omentum (Figure S1M). They are connected by a blood vessel to the spleen and superficially associated with the omentum, but not other surrounding organs, and easily removed intact with forceps (Figure S1M). Human melanoma frequently metastasizes to visceral organs (Kawashima et al., 1991; Trout et al., 2013). TA-TLS frequently develop in gut melanoma metastases but are infrequent in primary cutaneous tumors (Cipponi et al., 2012). Thus, I.P. B16 tumors are relevant models to study TA-TLS development.

To assess the impact of TA-TLSs on intratumoral immune cell composition, we compared $CD45^+$ cells from S.C. and I.P. tumors by flow cytometry. When normalized for tumor size, the numbers of DCs and CD8 and CD4 T cells were not significantly different (Figure 1B). In both tumor types, 92%–95% of CD8 and CD4 T cells were $CD62L^{neg}$, and thus antigen experienced (Figure 1C). Supporting this, 91%–94% of CD8 T cells and 65%–80% of CD4 T cells were $PD-1^+$. Most $CD62L^{neg}$ CD8 and CD4 T cells were also $CD44^{hi}$, again in keeping with an antigen-experienced phenotype (Figure 1D). However, I.P. tumors contained a larger fraction of $CD62L^{neg}$ $CD44^{lo}$ T cells, particularly in the CD4 compartment. These cells in both tumor types were largely $PD-1^+$, although this was more variable on S.C. $CD4^+$

T cells (Figure S2). Thus, despite being CD44^{lo}, they seem activated. Both tumors also contained small populations of CD62L⁺ CD44^{hi} presumptive central memory and CD62L⁺ CD44^{lo} naive cells (Figure 1D), and their expression of PD-1, LAG-3, and TIM-3 was consistent with this classification (Figure S2). However, I.P. tumors contained more naive and fewer central memory CD8 T cells than S.C. tumors, and this was more pronounced in the CD4 compartment (Figure 1D). These results suggest that TA-TLS in I.P. tumors enhance representation of naive and distinctly differentiated T cells, particularly CD4 T cells.

B cells from both tumor types were mainly B-2, and this was significantly enriched in I.P. relative to S.C. tumors (Figure 1E). This contrasts with the dominance of B-1 cells in the peritoneal cavity (Hayakawa et al., 1985) and omental fat-associated lymphoid clusters (FALC) (Cruz-Migoni and Caamaño, 2016) and suggests that the origin of B cells in TA-TLS and/or the factors driving their accumulation are distinct from those of these two peritoneal sites. Consistent with the large aggregates observed by IF, I.P. tumors contained ~20× more B cells than S.C. tumors. In both tumor types, the largest population was IgM⁺ IgD⁺ and presumptively naive (Figure 1F), and this population was significantly elevated in I.P. tumors. When normalized for size, I.P. tumors contained ~30× more naive, ~10× more presumptive class-switched (IgM^{neg} IgD^{neg}), and 8× more memory (IgM⁺ IgD^{neg}) B cells (Figure 1F). Thus, TA-TLS presence in I.P. tumors is associated with more robust B cell immunity and enhanced naive B cell representation.

A CAF population acts as LTo cells to orchestrate TA-TLS formation

When analyzed by flow cytometry, CD45⁺-depleted tumor suspensions contained many cells that were CD31^{neg} and podoplanin (PDPN) positive. PDPN is a conventional CAF marker (Pula et al., 2013), but B16 tumor cells express it at a low level (Figure S3A). However, only PDPN^{hi} cells expressed canonical CAF markers, particularly CD140α, Thy1, and fibroblast-activating protein (FAP) (Figure S3B), and these were analyzed as CAF in subsequent experiments. Thy1, FAP, and intracellular collagen type I (Col Type I) were all elevated on CAF from S.C. compared with I.P. tumors (Figure 2A and S3B), while α-smooth muscle actin (αSMA) expression was comparable (Figure S3C). I.P. tumors contained substantially more CAF than S.C. tumors, and a larger percentage expressed the proliferation marker Ki67⁺ (Figure 2B). Interestingly, the absolute number of FAP⁺ CAF was the same between S.C. and I.P. tumors (Figure 2B). Thus, the higher number of CAF in I.P. tumors is due to an expanded number of FAP^{neg} CAF.

CAF and tumor cells expressing high and low levels of PDPN, respectively, were also observed in tumor sections by IF. We established exposure times to visualize only PDPN bright CAF (Figure S3D). In S.C. tumors, CAF were scattered throughout the parenchyma (Figure 2C). In contrast, CAF in I.P. tumors formed reticular networks that were co-extensive with B and T cell aggregates of TA-TLS. By quantitative image analysis, CAF density in TA-TLS was substantially higher than in surrounding tumor parenchyma (Figure 2C), suggesting that their overall higher number in I.P. tumors was due to TA-TLS formation.

VCAM-1, ICAM-1, LT β R, and tumor necrosis factor receptors (TNFRs) I and II are canonical LTo cell markers (Mebius, 2003; Ruddle and Akirav, 2009; van de Pavert and Mebius, 2010). A larger fraction of I.P. CAF expressed TNFR I (Figure S3E) and LT β R (Figure 2D). Also, a significantly larger fraction of I.P. CAF expressed ICAM-1 and VCAM-1, and their surface expression levels were much higher (Figure 2D). The majority of I.P. CAF co-expressed ICAM-1 and VCAM-1, while those from S.C. tumors mainly expressed only ICAM-1 (Figure 2E). Although FDC-like cells are often found in TA-TLS, I.P. CAF did not express the FDC marker CD35 (Figure S3F). These results were consistent with the possibility that S.C. and I.P. tumors are dominated by mutually exclusive populations of CAF with FAP⁺ pro-tumor (Liu et al., 2019) and FAP^{neg} LTo phenotypes. However, even FAP⁺ CAF from I.P. tumors were much more likely to co-express VCAM-1 and ICAM-1 than FAP⁺ or FAP^{neg} CAF from S.C. tumors (Figure 2F). To provide more direct evidence for the association of these CAF populations with TA-TLS, we performed quantitative image analysis. Less than 15% of PDPN⁺ pixels in TA-TLS co-stained with FAP, while over 60% of those in the tumor parenchyma were FAP⁺, and their FAP expression was higher (Figure 2G). Conversely, 65%–70% of PDPN⁺ pixels in TA-TLS stained for VCAM-1 and ICAM-1, compared with only 25%–38% in the parenchyma, and their expression level was also higher (Figure 2H). Thus, despite the presence of both FAP⁺ and FAP^{neg} cells expressing ICAM-1 and VCAM-1 in I.P. tumors, the latter population is enriched in TA-TLSs, consistent with a role in TA-TLS development.

To directly test a role for CAF in orchestrating TA-TLS formation, we flow-sorted these cells from resected S.C. and I.P. tumors and injected them with B16-OVA cells into a S.C. site. The resulting tumors that contained CAF from S.C. tumors, or mouse embryonic fibroblasts, did not develop TA-TLS, lymphoid aggregates, or PDPN⁺ reticular networks (Figures 3A and 3B). Conversely, S.C. tumors that contained CAF from I.P. tumors contained PDPN⁺ reticular networks that were co-extensive with aggregates of B220⁺ B cells and CD3⁺ T cells and adjacent to PNAd⁺ vasculature (Figure 3A and 3B). Although the number of these structures and their size were significantly less than TA-TLS in I.P. tumors (Figure 3B), their composition, organization, and localization established them as TA-TLS. We also flow-sorted CAF from I.P. tumors grown in mice that ubiquitously express mCherry. When injected with B16-OVA cells, they persisted in the resulting s.c. tumors and were mainly found in TA-TLS (Figure 3C). Based on their association with TA-TLS (Figure 2G), we hypothesized that only FAP^{neg} CAF would promote TA-TLS formation. Indeed, when co-injected with B16-OVA cells, purified FAP^{neg} CAF promoted formation of small TA-TLS, analogous in size and number to those induced by bulk I.P. CAF (Figure 3D). FAP⁺ CAF induced less frequent and even smaller TA-TLS-like structures that were associated with PNAd but contained small numbers of poorly organized PDPN⁺ cells. These results establish that FAP^{neg} CAF from I.P. tumors act as surrogate LTo cells that promote TA-TLS formation. I.P. FAP⁺ CAF appear to have a minimal LTo capability that is nonetheless greater than that of S.C. CAF, suggesting that this property is induced by the I.P. tumor microenvironment.

We previously showed that both S.C. and I.P. CAF are a major source of CCL21 that recruits naive T cells (Peske et al., 2015). By quantitative real-time PCR, CAF from both tumor types expressed comparable levels of another homeostatic chemokine, CXCL12. However,

I.P. CAF expressed 5- to 10-fold higher levels of the B cell organizer chemokine CXCL13 and B cell survival factors BAFF and APRIL (Figure 3E). To provide direct evidence for the importance of CXCL13 in driving TA-TLS formation, we implanted I.P. tumors into mice lacking CXCR5, the cognate receptor for CXCL13. Although the numbers of TA-TLS in these tumors were comparable with those in wild-type (WT) tumors, they were significantly smaller (Figure 3F). This was associated with a reduced number of intratumoral B cells and CAF (Figures 3G and 3H). Significantly fewer of these CAF were proliferating, and the fraction co-expressing ICAM-1 and VCAM-1 was also reduced (Figure 3H). Thus, an intact CXCR5-CXCL13 chemotactic axis supports the proliferation of CAF with LTo characteristics and normal TA-TLS development.

Intratumoral CD8 T cells and B cells act coordinately as LTi cells driving TA-TLS development

We next investigated the roles of adaptive immune cells in TA-TLS development. I.P. tumors grown in Rag1^{-/-} mice lack PAd⁺ vasculature (Peske et al., 2015). These tumors also contained a smaller number of CAF than I.P. tumors from WT mice, which was similar to that of S.C. tumors (Figure 4A). These CAF were sometimes found in a low number of small, loosely organized clusters with CD45⁺ cells (Figure 4A; Figure S3G), which were not observed in WT S.C. tumors but did not form PDPN⁺ reticular networks. Per-cell expression of CCL21 and CXCL12 in CAF from these tumors was reduced by 11- and 6-fold, respectively, but that of CXCL13, BAFF, and APRIL was unchanged (Figure 4B). Per-cell expression of CXCL13, BAFF, and APRIL in CAF from I.P. tumors grown in Rag2^{-/-} IL2Rγ^{-/-} mice, which lack mature NK and ILC cells, was also comparable with that of CAF from WT mouse tumors (Figure S3H). Thus, CAF expression of molecules known to drive B cell accumulation and survival is controlled by a non-adaptive, non-NK, non-ILC element in the I.P. tumor microenvironment, but their accumulation and organization into reticular networks is controlled by adaptive immune cells.

To identify the adaptive immune cells driving CAF accumulation and organization, we utilized I.P. tumors grown in B cell-deficient μMT^{-/-} mice and in Rag1^{-/-} mice that had been repleted with bulk resting lymphocyte subpopulations prior to tumor implantation. Because these mice lack some TA-TLS elements, we evaluated tumors for PDPN⁺ reticular networks co-extensive with tightly organized aggregates of CD45⁺ cells. Tumors from μMT^{-/-} mice contained such organized CD45⁺/PDPN⁺ aggregates in numbers comparable with TA-TLS in WT mouse tumors, but they were significantly smaller (Figure 4C). Consistent with this, tumors from μMT^{-/-} mice had a lower density of CAF by IF and significantly fewer CAF by flow cytometry (Figure 4C). However, tumors from μMT^{-/-} and WT mice contained similar number of T cells and the small loosely organized CD45⁺/PDPN⁺ clusters (Figure S3I). I.P. tumors from Rag1^{-/-} mice repleted with CD8 T cells contained organized CD45⁺/PDPN⁺ aggregates similar in size and number to those in μMT^{-/-} mouse tumors (Figure 4D). Tumors from Rag1^{-/-} mice repleted with B cells contained an insignificantly different number of aggregates relative to tumors from unrepleted Rag1^{-/-} mice, although there was a slight increase in aggregate area. Importantly, tumors from Rag1^{-/-} mice repleted with both CD8 T cells and B cells resulted in structures comparable in number, size, and cellular composition and organization to

TA-TLS in WT mouse tumors. The area per section of the structures in tumors from these different recipients was reflected in the density of CAF (Figure 4D). Tumors from all of these mice contained a similar number of small, loosely organized CD45⁺/PDPN⁺ clusters (Figure S3G). Thus, T cells and B cells act as complementary LT_i cells mediating TA-TLS development: while T cells initiate reticular network formation, B cells drive expansion.

Intratumoral B cells drive TA-TLS expansion through LT β R signaling

LT β R signaling mediates the development of SLOs and some TLS. We found that I.P. tumors expressed significantly higher transcript levels of LT β R ligands LT α , LT β , and LIGHT than S.C. tumors (Figure S4A). To test their relevance, tumor-bearing mice were treated with an LT β R-Ig fusion protein, which binds LT $\alpha_1\beta_2$ and LIGHT and antagonizes LT β R signaling. Consistent with other work (Browning et al., 2005), LT β R-Ig treatment significantly reduced CXCL13 expression in tumor-reactive lymph nodes (Figure S4B). TA-TLSs in I.P. tumors from LT β R-Ig treated mice were comparable in number with WT mouse tumors, but significantly smaller, and these tumors contained fewer CAF (Figures 5A and 5B). Consistent with this, I.P. tumors from LT β R-Ig-treated mice contained fewer CD8 T cells and B cells, and the fractions of naive CD8 T cells, naive and central memory CD4 T cells, and naive B cells were significantly reduced (Figure 5C; Figures S4C–S4E). However, per-cell expression of CXCL13, BAFF, and APRIL in CAF from these tumors was unaffected (Figure 5D). Thus, LT β R signaling promotes expansion of TA-TLS-associated PDPN⁺ reticular networks, but not initial TA-TLS formation or CAF expression of LTO molecular characteristics.

Because CAF accumulation and reticular network expansion were impaired in the absence of either B cells or LT β R signaling, we tested whether it was mediated by LT $\alpha_1\beta_2$ ⁺ B cells. Tumors in Rag1^{-/-} mice repleted with WT CD8 T cells and LT α ^{-/-} B cells developed organized CD45⁺/PDPN⁺ aggregates comparable in size and number to those in tumors from Rag1^{-/-} mice repleted with CD8 T cells alone and in tumors from LT β R-Ig treated mice (Figure 5E). Also, the density of CAF in these tumor sections was comparable with I.P. tumors from Rag1^{-/-} mice repleted with CD8 T cells alone (Figure 5E). Tumors from all of these mice contained a similar number of small loosely organized CD45⁺/PDPN⁺ clusters (Figure S4F). Thus, CAF accumulation and TA-TLS expansion is mediated by intratumoral LT $\alpha_1\beta_2$ ⁺ B cells.

TNFR signaling promotes PDPN⁺ reticular network formation and expression of LTO molecules

Next, we determined whether TNFR signaling mediates TA-TLS development. In keeping with the models described above, we observed organized CD45⁺/PDPN⁺ aggregates in I.P. tumors grown in TNFR1/2^{-/-} mice that were smaller than TA-TLS in WT mouse tumors (Figure 5F). However, they were fewer, and the number of small loosely organized CD45⁺/PDPN⁺ clusters was also reduced (Figure S4G). As with TA-TLS in LT β R-Ig-treated mice, TNFR1/2^{-/-} mouse tumors contained fewer CAF (Figure 5G), and the fractions of naive CD4 and CD8 T cells were reduced (Figures S4H and S4I). These tumors also contained fewer B cells (Figure 5H), although the distribution of naive, class-switched and memory B cells was unaltered (Figure S4J). Most importantly, per-cell expression of CXCL13,

BAFF, and APRIL in CAF was substantially reduced (Figure 5I). These results demonstrate that TNFR signaling promotes PDPN⁺ reticular network development and LTo molecular characteristics of CAF.

Relationship of TA-TLS-associated i.p. CAF to peritoneal fibroblasts

The proximity of I.P. tumors to peritoneal organs suggested that CAF with LTo characteristics might derive from them. PDPN^{hi} cells from spleen, omentum, lung, pancreas, and skin of WT mice showed varying levels of CXCL13, BAFF, and APRIL expression (Figure S5). Similar to I.P. CAF, CXCL13 expression in PDPN^{hi} cells from the omentum was significantly reduced in TNFR1/2^{-/-} mice (Figure S5A) but was unaltered in cells from other organs (Figure S5A). However, in contrast with WT i.p. CAF, BAFF and APRIL expression was not reduced in PDPN^{hi} cells from any organ in TNFR1/2^{-/-} mice (Figures S5B and S5C). These results do not identify any peritoneal organ as the direct source of I.P. CAF. To the extent that they do originate from a peritoneal organ, they indicate that elements within the I.P. tumor microenvironment alter their TNFR-dependent expression of BAFF, APRIL, and in some cases, CXCL13.

Human TA-TLS contain elevated densities of LT⁺ B cells co-extensive with a reticular network of LTo-like CAF

To establish translational relevance of mechanisms driving murine TA-TLS development, we evaluated three human melanomas by quantitative image analysis using seven-color IF. We identified TA-TLS as aggregates of PNA⁺ cells, CD20⁺ B cells, CD8⁺ T cells, and gp36⁺ CAF (Figure 6A; Figure S6A). TA-TLS in all samples were enriched for APRIL⁺, VCAM-1⁺, and LT α ⁺ cells relative to the surrounding parenchyma, and TA-TLS in two samples showed higher densities of CXCL13⁺ cells (Figure 6B). TA-TLS in all samples were enriched for B cells expressing LT α , and these cells represented 60%–80% of the LT α ⁺ population inside the TA-TLS, as opposed to 0%–15% of those in the parenchyma (Figure 6C). TA-TLS in all samples also contained higher densities of CAF expressing APRIL⁺ and VCAM-1⁺ than the tumor parenchyma. The fraction of APRIL⁺ CAF was significantly higher in the TA-TLS of all samples, and the fraction of VCAM-1⁺ CAF was significantly higher in TA-TLS of two-thirds of samples (Figure 6C). However, only one sample showed higher densities of CXCL13⁺ CAF in TA-TLS, and there was no enrichment of CXCL13⁺ CAF in TA-TLS versus parenchyma (Figure 6C). The densities of B cells in TA-TLS strongly correlated with the densities of CAF overall and the densities of VCAM-1⁺ or APRIL⁺ CAF, but not those expressing CXCL13 (Figure 6D). However, the densities of B cells in TA-TLS also strongly correlated with the fractions of CAF in TA-TLS expressing VCAM-1 and APRIL, as well as CXCL13. Finally, the densities of LT α ⁺ B cells in TA-TLS correlated with the densities of CAF expressing VCAM-1 and APRIL, but not CXCL13. These results are consistent with the idea that human melanoma-associated TA-TLS are driven by similar cellular and molecular mechanisms as those driving murine TA-TLS development.

TA-TLS are associated with reduced tumor outgrowth and response to checkpoint immunotherapy

Increased number and size of TA-TLS strongly correlated with diminished i.p. tumor size in WT mice (Figure S7A), and deficiencies in TA-TLS development as a result of implantation into CXCR5^{-/-}, μ MT^{-/-}, LT β R-Ig-treated, and TNFR1/2^{-/-} mice were all associated with tumors that were significantly larger (170%–235%) than tumors in WT mice (Figure S7B). Also, a larger fraction of I.P. CAF expressed PD-L1 than their S.C. counterparts (Figure S7C). Thus, we assessed the impact of checkpoint immunotherapy on TA-TLS development and control of tumor outgrowth. We treated tumor-bearing WT mice with anti-PD-L1 monotherapy or the combination of anti-CTLA4 and anti-PD1 and analyzed tumors after 14 days of outgrowth. Both treatments increased intratumoral T cell numbers in both S.C. and I.P. tumors, but neither increased intratumoral B cell numbers nor promoted TA-TLS formation in S.C. tumors (Figures 7A and 7B). However, both treatments increased the number of intratumoral B cells in I.P. tumors. They also induced significant increases in TA-TLS number and size, suggesting that they initiate TA-TLS development and also operate on existing TA-TLS (Figures 7A–7C). Both treatments also promoted the development of TA-TLS with a “classical” (discrete T and B cell zones) organization (Figures 7B and 7C). Also, both treatments significantly reduced I.P. tumor size, but neither significantly reduced S.C. B16-OVA tumor size at this day 14 time point, despite the increased number of intratumoral T cells (Figure 7D). As with untreated mice, increased TA-TLS size and number were correlated with reduced tumor size. However, this correlation was more significant in both treatment groups (Figure 7E; Table S1). Similarly, B cell density correlated with reduced I.P. tumor size in untreated mice, and this correlation was also more significant in treated mice. In contrast, neither the density of total intratumoral T cells in S.C. or I.P. tumors nor the density of intratumoral B cells in S.C. tumors correlated with day 14 tumor size under any treatment condition (Figure 7E; Table S1). These results suggested that TA-TLS are an important determinant of anti-tumor activity in this model. To provide support for this hypothesis, we treated TNFR1/2^{-/-} mice bearing I.P. tumors in the same way. Both treatments again increased the number of intratumoral T and B cells at day 14 but did not promote TA-TLS development (Figures 7F and 7G). In contrast with WT mouse I.P. tumors, neither treatment reduced day 14 tumor size (Figure 7F), and the correlation between intratumoral B cell density and tumor size was lost (Figure 7H). These results demonstrate that checkpoint immunotherapy targets TA-TLS, leading to increases in their size and number. The extent of these changes is strongly correlated with tumor control. The potential importance of TA-TLS is heightened by a lack of correlation between tumor size and overall intratumoral T cell density.

DISCUSSION

This report identifies cellular and molecular mechanisms driving TA-TLS development in murine melanoma. A discrete population of CAF acquire LTo molecular characteristics in response to TNFR signals from a cell that is neither an adaptive nor innate immune lymphoid cell, and this population responds to intratumoral CD8 T cells and B cells that act coordinately as LT_i cells. Although CD8 T cells promote initial aggregation and reticular network formation, B cells are recruited by CXCL13 expressing CAF, subsequently driving

CAF proliferation and TA-TLS expansion through $LT\beta R$ signaling. Some of these cellular and molecular elements are overrepresented in human TA-TLS and associated with one another. Lastly, TA-TLS number, size, and organization increase in response to checkpoint immunotherapy, and these aspects of TA-TLS are strongly correlated with reduced tumor size. This work provides a platform for manipulating TA-TLS formation as a cancer immunotherapy strategy.

Our findings identify a previously undescribed role of a population of FAP^{neg} CAF as TA-TLS organizers. CAF that express elevated levels of FAP inversely correlate with patient survival, and their depletion results in diminished murine tumor outgrowth (Kraman et al., 2010). The numbers of FAP^+ CAF in both S.C. and I.P. tumors were comparable, and these cells were rarely found in TA-TLS. In contrast, FAP^{neg} CAF were elevated in I.P. tumors and the dominant population in TA-TLS reticular networks. FAP^{neg} CAF promoted TA-TLS development in non-TA-TLS-containing S.C. tumors. The number and size of these structures was lower than in I.P. tumors, and this may reflect constraints imposed by the S.C. tumor microenvironment. Both FAP^{neg} and FAP^+ CAF in i.p. tumors co-expressed ICAM-1 and VCAM-1 that were significantly higher than those expressed by FAP^+ CAF in S.C. tumors. In keeping with this, FAP^+ CAF from I.P. tumors have a minimal LTo capability that is nonetheless greater than that of CAF from S.C. tumors. Although $PDPN^+$ cells expressing elevated levels of ICAM-1 and VCAM-1 have been documented in TLSs associated with chronically inflamed tissues or murine pancreatic carcinoma (Peduto et al., 2009; Link et al., 2011), only a single report has demonstrated that such fibroblasts could support TLS formation in a murine model of Sjögren's syndrome, and these cells were FAP^+ (Nayar et al., 2019). It is possible that FAP^+ CAF from I.P. tumors express lower levels of CXCL13, BAFF, and APRIL than their FAP^{neg} counterparts, presumably as a consequence of TNFR signaling. These FAP^+ CAF may also be less proliferative than their FAP^{neg} counterparts. However, neither of these possibilities explains the observed differential accumulation of FAP^{neg} and FAP^+ CAF in TA-TLS and parenchyma, respectively. Our findings point to the importance of continuing work to characterize CAF subpopulations in different human tumors.

CAF can originate by trans-differentiation from tumor or endothelial cells, but typically from tissue resident $PDPN^+$ mesothelial cells (LeBleu and Kalluri, 2018; Liu et al., 2019). CAF in human and murine peritoneal carcinomas arise from $PDPN^+$ mesothelial cells lining the peritoneal cavity (Rynne-Vidal et al., 2015). The omentum contains a substantial number of $PDPN^+$ $CXCL13^+$ mesothelial cells (Jackson-Jones et al., 2020), and we identified $PDPN^+$ $CXCL13^+$ cells in the spleen, lung, and pancreas. Any or all of these cells could contribute to CAF in I.P. tumors, but none showed the TNFR-dependent regulation of BAFF and APRIL of I.P. tumor CAF. $PDPN^+$ cells from spleen, lung, and pancreas also did not show TNFR-dependent regulation of CXCL13. This suggests either another source of I.P. tumor CAF or changes in TNFR signaling in these populations under the influence of the tumor microenvironment. Regardless, the peritoneal cavity is a site for the growth or metastasis of many kinds of tumors, including melanoma (Kawashima et al., 1991; Trout et al., 2013). We also observed TA-TLS in tumors growing in lung, and $PDPN^+$ $CXCL13^+$ cells have been identified in several adipose tissues (Bénézech et al., 2015). Consequently,

we believe that this I.P. tumor model reflects a physiologically relevant TA-TLS biology that should be explored further.

Our results also provided insight into the mechanisms used by the CAF population to promote TA-TLS development. CAF from I.P. tumors expressed substantially higher levels of CXCL13, BAFF, and APRIL than those from S.C. tumors, and an intact CXCR5-CXCL13 axis promoted B cell accumulation in tumors and increased proliferation of CAF and TA-TLS expansion. Although B cell follicles are disrupted in CXCR5^{-/-} mice, the overall number of B cells in SLO is unaffected (Förster et al., 1996), making it likely that our result is due to a role for CXCL13 in promoting B cell accumulation. It is possible that CXCL13 enhances B cell proximity to CAF that express BAFF and APRIL, promoting B cell organization and/or survival in tumors. Elevated expression of CXCL13 is a common feature of TLS (Rangel-Moreno et al., 2007; Fleige et al., 2014; Barone et al., 2015; Sato et al., 2016), and fibroblasts purified from inflamed tissues containing TLS can express this molecule (Khader et al., 2011; Rangel-Moreno et al., 2011; Barone et al., 2015). The CXCR5-CXCL13 axis controls B cell accumulation in FALCs (Bénézech et al., 2015) and B cell organization, but not number, in TLS associated with a murine model of type 1 diabetes (Henry and Kendall, 2010). However, neither report identified the source of CXCL13. Although the precise mechanism by which CXCL13 promotes TLS development may vary based on anatomic location and/or immune stimulus, our results point to its central importance in TA-TLS formation in melanoma.

Our results also provide insight into the molecular and cellular control of CXCL13, BAFF, and APRIL expression in CAF. Expression of these molecules depended on signaling via TNFR, and not via LT β R, which controls them in SLO (Browning et al., 2005). Upregulation of CXCL13 in cultured smooth muscle cells from TLS-associated inflamed tissue was mediated by either LT β R or TNFR signaling alone, although the combination had a greater effect (Lötzer et al., 2010; Guedj et al., 2014). These differences point to the importance of determining the cellular sources of these LT-associated molecules, as well as the molecules that control their expression in additional TLS models and human diseases. Interestingly, we found that the expression of CXCL13, BAFF, and APRIL was not dependent on adaptive immune cells, NK cells, or ILCs. We previously showed that CCL21 expression depended on TNFR ligands expressed by effector CD8 T cells (Peske et al., 2015). Thus, although TNFR signaling induces expression of all of these molecules, they depend on different cell types expressing TNFR ligands. The cells responsible for TNFR-induced upregulation in CAF may be present and active only transiently during the course of tumor outgrowth, prior to the entry of CD8 effectors capable of upregulating CCL21 and PNA^d. Alternatively, because there are two TNFR isoforms that vary in their signaling pathways (MacEwan, 2002; Wajant and Siegmund, 2019) and their engagement with TNF- α and LT α_3 (Medvedev et al., 1996), it is possible that these two cell types signal via distinct receptor-ligand pairs.

We found that effector CD8 T cells and LT $\alpha_1\beta_2^+$ B cells act as complementary LT_i cells that coordinately induce TA-TLS development. While effector CD8 T cells promoted the organization of CAF into the reticular networks, along with upregulation of PNA^d and CCL21 (Peske et al., 2015), LT $\alpha_1\beta_2^+$ B cells drove CAF accumulation and TA-TLS

expansion. It has been shown that macrophages and NK cells can act as complementary LT_i, although their exact roles were not defined (Bénézech et al., 2015). However, a role for effector CD8 T cells in promoting TLS development has not been previously reported. LT β R signaling promotes TLS development in several infection/inflammation models, but LT $\alpha_1\beta_2^+$ B cells have been shown to act as LT_i only in development of isolated lymphoid follicles in small intestine, and this is independent of T cells (McDonald et al., 2005; Dubey et al., 2016). The presence of B cells in human tumors, particularly in association with TA-TLS, has a positive prognostic significance (Ladányi et al., 2011; Mahmoud et al., 2012; Cipponi et al., 2012; Germain et al., 2014), and it has been suggested that this is due to B cell activation and antibody production, or enhanced antigen-presenting cell function. Our results suggest that B cells might also promote tumor immunity by acting as LT_i cells to drive TA-TLS development.

The cellular and molecular elements driving murine TA-TLS development were also evident in TA-TLS of human melanoma. We identified LT α^+ B cells and APRIL⁺ and VCAM-1⁺ CAF as dominant components in human melanoma TA-TLS, and these phenotypes are suggestive of surrogate LT_i and L_{To} cells, respectively. Supporting this, the densities of LT α^+ B cells in TA-TLSs strongly correlated with the densities and fractions of CAF in TA-TLS expressing VCAM-1 and APRIL. How differences in cellular densities within TA-TLS influence their organization and functionality is not yet clear. Nonetheless, these data are consistent with our model in which LT α^+ B cells and L_{To} CAF promote one another's accumulation. The densities of B cells in TA-TLS strongly correlated with the fraction of CXCL13⁺ CAF, but not CXCL13⁺ CAF density. Also, CXCL13⁺ CAF were elevated in TA-TLS relative to parenchyma in only one of three melanomas, although the TA-TLS in two out of three melanomas contained elevated densities of CXCL13⁺ cells overall. This indicates the presence of alternative CXCL13-producing cells that are concentrated in the TA-TLS. CXCL13-expressing T_{FH} cells and CD8 T cells have been identified in human breast tumors and non-small cell lung cancer, respectively (Gu-Trantien et al., 2017; Thommen et al., 2018), and it is likely that such cells are also found in melanoma TA-TLS. Thus, although CXCL13 is likely to be an important contributor to human TA-TLS development, its cellular source may evolve over time.

Recent publications reported that TA-TLS presence prior to treatment was associated with a favorable response to immunotherapy in patients with cancer (Griss et al., 2019; Cabrita et al., 2020; Petitprez et al., 2020; Helmink et al., 2020). Although two of these papers associated TA-TLS “maturity” with measurements of activated B cells, none correlated TA-TLS maturity and clinical responses. One paper demonstrated that checkpoint immunotherapy was associated with an increase in intratumoral B cells, but no evident change in the number of TA-TLS. We identified a strong correlation between tumor control in response to checkpoint immunotherapy and TA-TLS development. In several genetic models in which TA-TLS development was compromised, average I.P. tumor size was significantly greater. The consistency of this observation coupled with the diversity of immune defects targeted suggests an association of tumor control with TA-TLS development. The number and size of TA-TLS in WT mice were strongly correlated with tumor size, suggesting that TA-TLS played a role in limiting tumor outgrowth. Most importantly, checkpoint immunotherapy of I.P., but not S.C., tumor-bearing mice promoted

tumor control, an increase in intratumoral B cell number, the development of more and larger TA-TLS, and the formation of TA-TLS with discrete T and B cell compartments. Intratumoral B cell number and TA-TLS size and number in checkpoint immunotherapy-treated mice were even more significantly correlated with a reduction in tumor size than in control mice. Although checkpoint immunotherapy also increased the overall number of intratumoral T cells, there was no correlation between these numbers and size of either I.P. or S.C. tumors. I.P. tumor control was lost in both untreated and treated TNFR1/2^{-/-} mice, which lack TA-TLS, despite an increase in parenchymal T cell accumulation similar to that of WT mice. Multivariate studies in non-small cell lung cancer (Goc et al., 2014) and colorectal cancer (Di Caro et al., 2014) have also established a beneficial prognostic value of TA-TLS independent of TIL density. Although it is possible that checkpoint blockade-induced tumor control in TNFR1/2^{-/-} mice is compromised for other reasons, these mice develop normal SLO and have a normal immune cell distribution and number (Peschon et al., 1998). Additionally, these mice generate adequate effector T cells (Peske et al., 2015), and total T cell infiltration into tumors in WT and TNFR1/2^{-/-} mice was similar. We do not assert that S.C. B16-OVA tumors lacking TLS are entirely unresponsive to checkpoint immunotherapy, as there is evidence of this in other studies, albeit with considerable variation (Binder et al., 2013; Curran et al., 2010; Perez-Ruiz et al., 2019; Stark et al., 2017; Reilley et al., 2019; De Henau et al., 2016; Heidegger et al., 2019; Miller et al., 2019). Their response may be delayed relative to that of I.P. tumors that contain TA-TLS, or it may be quantitatively smaller. Regardless, in our model on day 14, it is simply not evident, either as an effect on tumor size or in the association between tumor size and the number of infiltrating B and T cells. We reach a similar conclusion regarding I.P. tumors grown in TNFR1/2^{-/-} mice. Collectively, our work suggests that TA-TLS are major targets of checkpoint immunotherapy, and their presence and organization may be important determinants of the antitumor immune response engendered by this treatment. This conclusion supports and extends conclusions reached in correlative studies in patients.

STAR★METHODS

RESOURCE AVAILABILITY

Lead contact—Further information, and request for resources and reagents should be directed to the lead contact, Dr. Victor H. Engelhard (vhe@virginia.edu)

Materials availability—This study did not generate any unique reagents or mouse lines.

Data and code availability—This paper does not report original datasets.

This paper does not report original code.

Any additional information required to reanalyze the data reported in this paper is available from the lead contact upon request

EXPERIMENTAL MODEL AND SUBJECT DETAILS

Animal models—Mice used in this study and their respective vendor are detailed in Key resources table. All mice were bred and maintained on a C57BL/6 background, and kept

in specific pathogen-free conditions. All experiments were carried out on female mice that were ~8–12 weeks of age. All protocols and experiments were approved by the University of Virginia Institutional Animal Care and Use Committee.

Tumor models—B16-F1 mouse melanoma and MC38 murine colon adenocarcinoma cells were obtained from American Type Culture Collection (ATCC). The generation of B16-OVA and MC38-OVA has previously been described (Hargadon et al., 2006). B16-OVA tumor cells were cultured in RPMI-1640 (Corning) supplemented to a final concentration of 10% (v/v) fetal bovine serum (FBS), 2 mM L-glutamine (ThermoFisher Scientific) and 15 mM HEPES (ThermoFisher Scientific). MC38-OVA were cultured in DMEM (Corning) supplemented to a final concentration of 10% (v/v) FBS, 2 mM L-glutamine (ThermoFisher Scientific) and 15 mM HEPES (ThermoFisher Scientific). Lewis lung carcinoma transfected to express ovalbumin (LLC-OVA) was a gift of Dr. E. Podack (University of Miami). These cells were cultured in IMDM (ThermoFisher Scientific) supplemented to a final concentration of 10% (v/v) fetal bovine serum, 2 mM L-glutamine (ThermoFisher Scientific) and 15 mM HEPES (ThermoFisher Scientific). All tumor cells were cultured and maintained at 37°C and 5% carbon dioxide. For tumor studies, approximately 4×10^5 tumor cells were I.P. or S.C. (loose neck scruff) injected into recipient mice. Both tumor types were allowed to establish for 14 days prior to harvesting.

METHOD DETAILS

Treatment of tumor-bearing mice—For LT β R blocking experiments, LT β R-Ig fusion protein (Wu et al., 1999) (100 μ g per injection, gift from Y.X.F) was injected I.P. into C57BL/6 mice one day prior and one day after tumor implantation, and then every four days until tumor harvest. For checkpoint immunotherapy experiments, either monotherapy α -PDL1 (250 μ g per injection, 10F.9G2, BioXcell) or dual therapy α -PD1 (250 μ g per injection, RMP1–14, BioXcell) and α -CTLA4 (250 μ g per injection, 9D9, BioXcell) was injected I.P. into C57BL/6 mice three days after tumor implantation and then every three days until tumor harvest.

Adoptive transfer of T cells and B cells—Lymph nodes and/or spleen were resected from either C57BL/6 or LT $\alpha^{-/-}$ mice. Single-cell suspensions of resected lymphoid organs were prepared via Dounce homogenization. Bulk CD8 T cells and CD19 B cells were purified from pooled lymph nodes and/or spleen suspensions by magnetic bead isolation kits (Miltenyi Biotec) on an AutoMACS Pro Separator (Miltenyi Biotec) according to manufactures instructions. CD8 T cells (5×10^6), CD19 B cells (5×10^6), or the combination were injected intravenously into Rag1 $^{-/-}$ recipient mice 3 days prior to tumor implantation.

Digestion of resected tissues—Resected lymph nodes, spleen, omentum, lung, pancreas, skin, and tumors were minced and digested with a solution containing 0.1 mg/ml DNase I (Sigma), 0.8 mg/ml Collagenase Dispase (Sigma), and 0.2 mg/ml Collagenase P (Sigma) for 30 minutes at 37°C. Every 5 minutes, tissue suspensions were pipetted up-and-down several times. Digested tissues were depleted of red blood cells by Red Blood Cell Lysing Buffer Hybri-Max (Sigma) according to manufactures instructions.

Enrichment of cells from digested tissues—Hematopoietic cells from digested tumor suspensions were enriched by CD45 magnetic beads (Miltenyi Biotec) on an AutoMACS Pro Separator (Miltenyi Biotec) according to manufactures instructions. In some cases, hematopoietic depleted tissue suspensions were stained with α -gp38 (0.5 μ g/mL) biotinylated antibody for 15 minutes at 4°C. Then, CAF and tissue resident fibroblasts were enriched from stained hematopoietic depleted suspensions by α -biotin magnetic beads (Miltenyi Biotec) on an AutoMACS Pro Separator (Miltenyi Biotec) according to manufactures instructions.

Flow cytometry and cell sorting—Antibodies used for flow cytometry analysis are detailed in Key resources table. Cell surface staining was done in PBS containing 2% FBS, 2 mM EDTA (Sigma), and 2 mM NaN₃ (Sigma) for 30 minutes at 4°C. For the detection of intracellular proteins, Cytofix/Cytoperm Fixation/Permeabilization kit (BD Bioscience) or Transcription Faactor Buffer Set (BD Bioscience) was used according to the manufacturer's instructions. Live/Dead Aqua (Invitrogen) or 4,6-diamidino-2-phenylindole (Sigma) were used to exclude dead cells from analysis. In all experiments, CAF and/or tissue derived fibroblasts were defined as live, singlet, Ter119^{neg}, CD45^{neg}, CD31^{neg}, PDPN^{hi} cells. B16 tumor cells express ten-fold lower levels of PDPN. Thus, only PDPN^{hi} cells were analyzed as CAF in all experiments. Samples were run on a FACSCanto II (BD) or Attune NxT (ThermoFisher/Invitrogen) and analyzed using FlowJo Software (BD Bioscience). For quantitative real-time PCR experiments, pre-enriched CAF and/or organ derived fibroblasts were sorted to high purity on an Influx Cell Sorter (BD) directly into RNAProtect (QIAGEN) or PBS.

S.C. tumor model with exogenous fibroblasts—B16-OVA cells were S.C. or I.P. injected into female C57BL/6 or UBC-mCherry recipient mice and allowed to establish for 14 days. Preparation of single cell suspensions from resected tumor masses is described above. Live, singlet, Ter119⁻, CD45⁻, CD31⁻, PDPN^{hi} CAF from pre-enriched suspensions of bulk PDPN⁺ CAF were sorted to high purity on Influx Cell Sorter (BD) directly into DMEM (Corning) supplemented to a final concentration of 10% (v/v) FBS, 2 mM L-glutamine (ThermoFisher Scientific) and 15 mM HEPES (ThermoFisher Scientific). In some cases, FAP⁺ PDPN^{hi} and FAP^{neg} PDPN^{hi} CAF were purified from a pre-enriched suspension of bulk PDPN⁺ CAFs were sorted to high purity on Influx Cell Sorter (BD) directly into DMEM (Corning) supplemented to a final concentration of 10% (v/v) FBS, 2 mM L-glutamine (ThermoFisher Scientific) and 15 mM HEPES (ThermoFisher Scientific). In all cases, B16-OVA cells (4×10^5) and purified CAF (5×10^4) or mouse embryonic fibroblasts (5×10^4) were S.C. injected into female C57BL/6 mice. Tumor were allowed to establish for 14 days prior to harvesting.

Immunofluorescence microscopy—Antibodies used for immunofluorescence microscopy (IF) analysis are detailed in Key resources table. Preparation of tumor tissue for frozen sectioning, immunofluorescence staining procedures, and Tyramide signal amplification (PerkinElmer) for PNAd detections has previously been described (Rodriguez et al., 2018). For image acquisition, 10–15 low magnification images per tumor section were used for TA-TLS, CAF and intratumoral T-/B cell quantification. For the detection

of intratumoral CAF, exposure times and thresholds were set to visualize bright PDPN⁺ cells located in perivascular and TA-TLS areas, while eliminating the dim tumor cell signal. For CAF and LTo marker expression on intratumoral fibroblasts, the average of five high magnification images per parenchyma and TA-TLS area of a tumor section were used for quantification. All images were captured on an AxioImager with Apotome (Zeiss) and images were analyzed either by ImageJ Software (NIH) or Imaris image analysis software (Bitplane). For image presentation, brightness and contrast were linearly adjusted and color-merged images were generated using Photoshop CS6 Software (Adobe).

Definition of TA-TLS by IF—In I.P. tumors grown in C57BL/6, CXCR5^{-/-}, LTβR-Ig and checkpoint treated mice, and in S.C. tumors containing PDPN⁺ CAF or mouse embryonic fibroblasts, intratumoral TA-TLS were identified as tight aggregates of 50 or more B cells in juxtaposition to PNA⁺ vasculature and associated with a reticular network of elongated PDPN⁺ CAF that are not tightly apposed to tumor endothelium (Rodriguez et al., 2018). T cells and DC were either intermingled with B cell aggregates (non-classical structure) or organized as a separate zone (classical structure). Using an AxioImager with Apotome (Zeiss) and ImageJ Software (NIH) or Imaris image analysis software (Bitplane), B cell and PDPN staining pattern were used to draw a boundary of the TA-TLS, and quantitate its surface area.

In I.P. tumors grown in μMT^{-/-}, TNFR1/2^{-/-}, or in I.P. tumors grown in Rag1^{-/-} mice repleted with bulk CD8 T cells and/or B cells, we identified tight clusters of CD45⁺ –hematopoietic cells associated with a network of elongated PDPN⁺ CAF that were not tightly apposed to tumor endothelium as elements of TA-TLS development. Using an AxioImager with Apotome (Zeiss) and ImageJ Software (NIH), clusters of CD45⁺ and PDPN⁺ staining pattern is used to draw a boundary and quantitate its surface area.

Multispectral Imaging—Antibodies used for multispectral imaging analysis are detailed in Key resources table. Staining of murine and human melanoma for multispectral imaging has previously been described (Mauldin et al., 2020). In brief, 4-μm thick sections were cut from formalin fixed paraffin embedded murine tumor specimens or human melanoma biopsies, and murine spleen and human lymph node biopsies was used as a positive control. Antigen retrieval was performed using AR9 buffer (PerkinElmer) according to the manufacturer instructions. OPAL Multiplex IHC Staining (PerkinElmer) was performed according to the manufacturer instructions. Slides were mounted using prolong diamond antifade (Life Technologies) and scanned at low magnification using the Vectra 3.0 system and software (PerkinElmer). Regions of interest were identified in Phenochart software, and high-powered magnification images were acquired with the Vectra 3.0 system (Akoya Biosciences). These images were spectrally unmixed using single stain positive controls and analyzed using the InForm software (PerkinElmer). Human specimen images were quantified using HALO software (Indica Labs, Albuquerque, NM) and murine specimens were quantified by eye.

Quantitative real-time PCR—Probes used for quantitative real-time PCR analysis are detailed in Key resources table. RNA was purified from whole tumor or sorted cells using RNeasy kits (QIAGEN) according to manufactures instructions. High-Capacity cDNA

Reverse Transcription Kit (Applied Biosystems) and purified RNA was used to generate cDNA. Amplification was performed using TaqMan Fast Advanced Master Mix (Applied Biosystems) and QuantStudio 6 Flex Real-Time PCR system (Applied Biosystems) with the following program: 50°C for 2 minutes; 95°C for 2 minutes; 40 cycles of 95°C for 1 s, 60°C for 20 s. Data is presented as 2^{-Ct} relative to *Hprt*.

QUANTIFICATION AND STATISTICAL ANALYSIS

Statistical details of each experiment in this work are reported in the main and supplementary figure legends. P values are shown in each figure, and defined in the associated figure legend. Normality of data distribution was determined by D'Agostino-Pearson omnibus normality test and variance between groups was assessed by the *F*-test. P values for the comparison between two or more independent groups were calculated by Welch's t test and Kruskal-Wallis *h*-test with Dunn's post-test, respectively. For human boxplot data, the Wilcoxon rank-sum test was used for non-parametric comparison of two independent groups, and P values were corrected by controlling the False Discovery Rate (FDR) according to the method of Benjamini and Hochberg. For human correlation analysis, a linear mixed-models approach available in the R package *Correlations* (Makowski et al., 2020) was used in order to account for the nested data structure (multiple data points taken from an independent tumor). For murine checkpoint immunotherapy correlation analysis, a Spearman correlation analysis with 95% confidence intervals was used for the non-parametric comparison of two independent groups. In most cases, error bars shown in graphical data represents mean \pm standard deviation (s.d.) for normally distributed data or median \pm IQR for non-normal data. For human boxplots, data were generated using Tukey's method. $p < 0.05$ was considered statistically significant. All graphs and statistics were calculated using Graph Pad Prism version 7.0, R version 4, and the SAS software suite version 9.4.

Supplementary Material

Refer to Web version on PubMed Central for supplementary material.

ACKNOWLEDGMENTS

We thank the Engelhard and Dudley labs for discussion and suggestions. This work was supported by USPHS Grants CA78400 and CA181794 (to V.H.E.) and the University of Virginia Cancer Center Schiff Foundation (to C.L.S. and I.S.M.). The University of Virginia Histology and Flow Cytometry Cores are supported by USPHS Grant P30 CA44579. A.B.R. and A.N.W. were supported by USPHS Training Grant AI007496, J.D.P. by USPHS Training Grant GM007267, and K.M.L. by USPHS Training Grant CA163177. J.D.P. was the recipient of a Farrow Fellowship, and A.B.R. was the recipient of a Wagner Fellowship, both from the University of Virginia.

REFERENCES

- Barone F, Nayar S, Campos J, Cloake T, Withers DR, Toellner K-M, Zhang Y, Fouser L, Fisher B, Bowman S, et al. (2015). IL-22 regulates lymphoid chemokine production and assembly of tertiary lymphoid organs. *Proc. Natl. Acad. Sci. USA* 112, 11024–11029. [PubMed: 26286991]
- Bénézech C, Luu N-T, Walker JA, Kruglov AA, Loo Y, Nakamura K, Zhang Y, Nayar S, Jones LH, Flores-Langarica A, et al. (2015). Inflammation-induced formation of fat-associated lymphoid clusters. *Nat. Immunol* 16, 819–828. [PubMed: 26147686]

- Binder DC, Engels B, Arina A, Yu P, Slauch JM, Fu Y-X, Karrison T, Burnette B, Idel C, Zhao M, et al. (2013). Antigen-specific bacterial vaccine combined with anti-PD-L1 rescues dysfunctional endogenous T cells to reject long-established cancer. *Cancer Immunol. Res* 1, 123–133. [PubMed: 24455752]
- Bombardieri M, Barone F, Humby F, Kelly S, McGurk M, Morgan P, Challacombe S, De Vita S, Valesini G, Spencer J, and Pitzalis C (2007). Activation-induced cytidine deaminase expression in follicular dendritic cell networks and interfollicular large B cells supports functionality of ectopic lymphoid neogenesis in autoimmune sialoadenitis and MALT lymphoma in Sjögren's syndrome. *J. Immunol* 179, 4929–4938. [PubMed: 17878393]
- Browning JL, Allaire N, Ngam-Ek A, Notidis E, Hunt J, Perrin S, and Fava RA (2005). Lymphotoxin-beta receptor signaling is required for the homeostatic control of HEV differentiation and function. *Immunity* 23, 539–550. [PubMed: 16286021]
- Cabrita R, Lauss M, Sanna A, Donia M, Skaarup Larsen M, Mitra S, Johansson I, Phung B, Harbst K, Vallon-Christersson J, et al. (2020). Tertiary lymphoid structures improve immunotherapy and survival in melanoma. *Nature* 577, 561–565. [PubMed: 31942071]
- Cañete JD, Celis R, Yeremenko N, Sanmartí R, van Duivenvoorde L, Ramírez J, Blijdorp I, García-Herrero CM, Pablos JL, and Baeten DL (2015). Ectopic lymphoid neogenesis is strongly associated with activation of the IL-23 pathway in rheumatoid synovitis. *Arthritis Res. Ther* 17, 173. [PubMed: 26156866]
- Cipponi A, Mercier M, Seremet T, Baurain J-F, Théate I, van den Oord J, Stas M, Boon T, Coulie PG, and van Baren N (2012). Neogenesis of lymphoid structures and antibody responses occur in human melanoma metastases. *Cancer Res.* 72, 3997–4007. [PubMed: 22850419]
- Cruz-Migoni S, and Caamaño J (2016). Fat-associated lymphoid clusters in inflammation and immunity. *Front. Immunol* 7, 612. [PubMed: 28066422]
- Curran MA, Montalvo W, Yagita H, and Allison JP (2010). PD-1 and CTLA-4 combination blockade expands infiltrating T cells and reduces regulatory T and myeloid cells within B16 melanoma tumors. *Proc. Natl. Acad. Sci. USA* 107, 4275–4280. [PubMed: 20160101]
- De Henau O, Rausch M, Winkler D, Campesato LF, Liu C, Cymerman DH, Budhu S, Ghosh A, Pink M, Tchaicha J, et al. (2016). Overcoming resistance to checkpoint blockade therapy by targeting PI3K γ in myeloid cells. *Nature* 539, 443–447. [PubMed: 27828943]
- Di Caro G, Bergomas F, Grizzi F, Doni A, Bianchi P, Malesci A, Laghi L, Allavena P, Mantovani A, and Marchesi F (2014). Occurrence of tertiary lymphoid tissue is associated with T-cell infiltration and predicts better prognosis in early-stage colorectal cancers. *Clin. Cancer Res* 20, 2147–2158. [PubMed: 24523438]
- Drayton DL, Ying X, Lee J, Lesslauer W, and Ruddle NH (2003). Ectopic LT α β directs lymphoid organ neogenesis with concomitant expression of peripheral node addressin and a HEV-restricted sulfotransferase. *J. Exp. Med* 197, 1153–1163. [PubMed: 12732657]
- Dubey LK, Lebon L, Mosconi I, Yang C-Y, Scandella E, Ludewig B, Luther SA, and Harris NL (2016). Lymphotoxin-Dependent B Cell-FRC Crosstalk Promotes De Novo Follicle Formation and Antibody Production following Intestinal Helminth Infection. *Cell Rep.* 15, 1527–1541. [PubMed: 27160906]
- Engelhard VH, Rodriguez AB, Mauldin IS, Woods AN, Peske JD, and Slingluff CL Jr. (2018). Immune Cell Infiltration and Tertiary Lymphoid Structures as Determinants of Antitumor Immunity. *J. Immunol* 200, 432–442. [PubMed: 29311385]
- Finkin S, Yuan D, Stein I, Taniguchi K, Weber A, Unger K, Browning JL, Goossens N, Nakagawa S, Gunasekaran G, et al. (2015). Ectopic lymphoid structures function as microniches for tumor progenitor cells in hepatocellular carcinoma. *Nat. Immunol* 16, 1235–1244. [PubMed: 26502405]
- Fleige H, Ravens S, Moschovakis GL, Bölter J, Willenzon S, Sutter G, Häussler S, Kalinke U, Prinz I, and Förster R (2014). IL-17-induced CXCL12 recruits B cells and induces follicle formation in BALT in the absence of differentiated FDCs. *J. Exp. Med* 211, 643–651. [PubMed: 24663215]
- Förster R, Mattis AE, Kremmer E, Wolf E, Brem G, and Lipp M (1996). A putative chemokine receptor, BLR1, directs B cell migration to defined lymphoid organs and specific anatomic compartments of the spleen. *Cell* 87, 1037–1047. [PubMed: 8978608]

- Furtado GC, Marinkovic T, Martin AP, Garin A, Hoch B, Hubner W, Chen BK, Genden E, Skobe M, and Lira SA (2007). Lymphotoxin beta receptor signaling is required for inflammatory lymphangiogenesis in the thyroid. *Proc. Natl. Acad. Sci. USA* 104, 5026–5031. [PubMed: 17360402]
- Furtado GC, Pacer ME, Bongers G, Bénézec C, He Z, Chen L, Berin MC, Kollias G, Caamaño JH, and Lira SA (2014). TNF α -dependent development of lymphoid tissue in the absence of ROR γ ⁺ lymphoid tissue inducer cells. *Mucosal Immunol.* 7, 602–614. [PubMed: 24129162]
- Gatumu MK, Skarstein K, Papandile A, Browning JL, Fava RA, and Bolstad AI (2009). Blockade of lymphotoxin-beta receptor signaling reduces aspects of Sjögren's syndrome in salivary glands of non-obese diabetic mice. *Arthritis Res. Ther* 11, R24. [PubMed: 19222863]
- Germain C, Gnjjatic S, Tamzalit F, Knockaert S, Remark R, Goc J, Lepelley A, Becht E, Katsahian S, Bizouard G, et al. (2014). Presence of B cells in tertiary lymphoid structures is associated with a protective immunity in patients with lung cancer. *Am. J. Respir. Crit. Care Med* 189, 832–844. [PubMed: 24484236]
- GeurtsvanKessel CH, Willart MA, Bergen IM, van Rijt LS, Muskens F, Elewaut D, Osterhaus AD, Hendriks R, Rimmelzwaan GF, and Lambrecht BN (2009). Dendritic cells are crucial for maintenance of tertiary lymphoid structures in the lung of influenza virus-infected mice. *J. Exp. Med* 206, 2339–2349. [PubMed: 19808255]
- Goc J, Germain C, Vo-Bourgais TKD, Lupo A, Klein C, Knockaert S, de Chaisemartin L, Ouakrim H, Becht E, Alifano M, et al. (2014). Dendritic cells in tumor-associated tertiary lymphoid structures signal a Th1 cytotoxic immune contexture and license the positive prognostic value of infiltrating CD8⁺ T cells. *Cancer Res.* 74, 705–715. [PubMed: 24366885]
- Goya S, Matsuoka H, Mori M, Morishita H, Kida H, Kobashi Y, Kato T, Taguchi Y, Osaki T, Tachibana I, et al. (2003). Sustained interleukin-6 signalling leads to the development of lymphoid organ-like structures in the lung. *J. Pathol* 200, 82–87. [PubMed: 12692845]
- Gräbner R, Lötzer K, Döpping S, Hildner M, Radke D, Beer M, Spanbroek R, Lippert B, Reardon CA, Getz GS, et al. (2009). Lymphotoxin β receptor signaling promotes tertiary lymphoid organogenesis in the aorta adventitia of aged ApoE^{-/-} mice. *J. Exp. Med* 206, 233–248. [PubMed: 19139167]
- Griss J, Bauer W, Wagner C, Simon M, Chen M, Grabmeier-Pfisters-hammer K, Maurer-Granofszky M, Roka F, Penz T, Bock C, et al. (2019). B cells sustain inflammation and predict response to immune checkpoint blockade in human melanoma. *Nat. Commun* 10, 4186. [PubMed: 31519915]
- Gu-Trantien C, Migliori E, Buisseret L, de Wind A, Brohé S, Garaud S, Noël G, Dang Chi VL, Lodewyckx J-N, Naveaux C, et al. (2017). CXCL13-producing T_{FH} cells link immune suppression and adaptive memory in human breast cancer. *JCI Insight* 2, e91487.
- Guedj K, Khallou-Laschet J, Clement M, Morvan M, Gaston A-T, Fornasa G, Dai J, Gervais-Taurel M, Eberl G, Michel J-B, et al. (2014). M1 macrophages act as LT β R-independent lymphoid tissue inducer cells during atherosclerosis-related lymphoid neogenesis. *Cardiovasc. Res* 101, 434–443. [PubMed: 24272771]
- Halle S, Dujardin HC, Bakocevic N, Fleige H, Danzer H, Willenzon S, Suezer Y, Hämmerling G, Garbi N, Sutter G, et al. (2009). Induced bronchus-associated lymphoid tissue serves as a general priming site for T cells and is maintained by dendritic cells. *J. Exp. Med* 206, 2593–2601. [PubMed: 19917776]
- Hargadon KM, Brinkman CC, Sheasley-O'neill SL, Nichols LA, Bullock TNJ, and Engelhard VH (2006). Incomplete differentiation of antigen-specific CD8 T cells in tumor-draining lymph nodes. *J. Immunol* 177, 6081–6090. [PubMed: 17056534]
- Hayakawa K, Hardy RR, Herzenberg LA, and Herzenberg LA (1985). Progenitors for Ly-1 B cells are distinct from progenitors for other B cells. *J. Exp. Med* 161, 1554–1568. [PubMed: 3874257]
- Heidegger S, Wintges A, Stritzke F, Bek S, Steiger K, Koenig P-A, Göttert S, Engleitner T, Öllinger R, Nedelko T, et al. (2019). RIG-I activation is critical for responsiveness to checkpoint blockade. *Sci. Immunol* 4, eaau8943. [PubMed: 31519811]
- Helmink BA, Reddy SM, Gao J, Zhang S, Basar R, Thakur R, Yizhak K, Sade-Feldman M, Blando J, Han G, et al. (2020). B cells and tertiary lymphoid structures promote immunotherapy response. *Nature* 577, 549–555. [PubMed: 31942075]

- Henry RA, and Kendall PL (2010). CXCL13 blockade disrupts B lymphocyte organization in tertiary lymphoid structures without altering B cell receptor bias or preventing diabetes in nonobese diabetic mice. *J. Immunol* 185, 1460–1465. [PubMed: 20574003]
- Jackson-Jones LH, Smith P, Portman JR, Magalhaes MS, Mylonas KJ, Vermeren MM, Nixon M, Henderson BEP, Dobie R, Vermeren S, et al. (2020). Stromal Cells Covering Omental Fat-Associated Lymphoid Clusters Trigger Formation of Neutrophil Aggregates to Capture Peritoneal Contaminants. *Immunity* 52, 700–715.e6. [PubMed: 32294409]
- Johansson-Percival A, He B, Li Z-J, Kjellén A, Russell K, Li J, Larma I, and Ganss R (2017). De novo induction of intratumoral lymphoid structures and vessel normalization enhances immunotherapy in resistant tumors. *Nat. Immunol* 18, 1207–1217. [PubMed: 28892469]
- Joshi NS, Akama-Garren EH, Lu Y, Lee D-Y, Chang GP, Li A, Du-Page M, Tammela T, Kerper NR, Farago AF, et al. (2015). Regulatory T cells in tumor-associated tertiary lymphoid structures suppress anti-tumor T cell responses. *Immunity* 43, 579–590. [PubMed: 26341400]
- Kawashima A, Fishman EK, Kuhlman JE, and Schuchter LM (1991). CT of malignant melanoma: patterns of small bowel and mesenteric involvement. *J. Comput. Assist. Tomogr* 15, 570–574. [PubMed: 2061469]
- Khader SA, Guglani L, Rangel-Moreno J, Gopal R, Junecko BAF, Fountain JJ, Martino C, Pearl JE, Tighe M, Lin YY, et al. (2011). IL-23 is required for long-term control of Mycobacterium tuberculosis and B cell follicle formation in the infected lung. *J. Immunol* 187, 5402–5407. [PubMed: 22003199]
- Kim H-J, Kammertoens T, Janke M, Schmetzer O, Qin Z, Berek C, and Blankenstein T (2004). Establishment of early lymphoid organ infrastructure in transplanted tumors mediated by local production of lymphotoxin α and in the combined absence of functional B and T cells. *J. Immunol* 172, 4037–4047. [PubMed: 15034015]
- Kirk CJ, Hartigan-O'Connor D, and Mulé JJ (2001). The dynamics of the T-cell antitumor response: chemokine-secreting dendritic cells can prime tumor-reactive T cells extranodally. *Cancer Res.* 61, 8794–8802. [PubMed: 11751401]
- Koenig A, and Thauinat O (2016). Lymphoid Neogenesis and Tertiary Lymphoid Organs in Transplanted Organs. *Front. Immunol* 7, 646. [PubMed: 28082981]
- Kraman M, Bambrough PJ, Arnold JN, Roberts EW, Magiera L, Jones JO, Gopinathan A, Tuveson DA, and Fearon DT (2010). Suppression of antitumor immunity by stromal cells expressing fibroblast activation protein- α . *Science* 330, 827–830. [PubMed: 21051638]
- Ladányi A, Kiss J, Mohos A, Somlai B, Liszky G, Gilde K, Fejös Z, Gaudi I, Dobos J, and Tímár J (2011). Prognostic impact of B-cell density in cutaneous melanoma. *Cancer Immunol. Immunother* 60, 1729–1738. [PubMed: 21779876]
- LeBleu VS, and Kalluri R (2018). A peek into cancer-associated fibroblasts: origins, functions and translational impact. *Dis. Model. Mech* 11, dmm029447. [PubMed: 29686035]
- Lee JJ, McGarry MP, Farmer SC, Denzler KL, Larson KA, Carrigan PE, Brenneise IE, Horton MA, Haczku A, Gelfand EW, et al. (1997). Interleukin-5 expression in the lung epithelium of transgenic mice leads to pulmonary changes pathognomonic of asthma. *J. Exp. Med* 185, 2143–2156. [PubMed: 9182686]
- Link A, Hardie DL, Favre S, Britschgi MR, Adams DH, Sixt M, Cyster JG, Buckley CD, and Luther SA (2011). Association of T-zone reticular networks and conduits with ectopic lymphoid tissues in mice and humans. *Am. J. Pathol* 178, 1662–1675. [PubMed: 21435450]
- Liu T, Han C, Wang S, Fang P, Ma Z, Xu L, and Yin R (2019). Cancer-associated fibroblasts: an emerging target of anti-cancer immunotherapy. *J. Hematol. Oncol* 12, 86. [PubMed: 31462327]
- Lötzer K, Döpping S, Connert S, Gräbner R, Spanbroek R, Lemser B, Beer M, Hildner M, Hehlhans T, van der Wall M, et al. (2010). Mouse aorta smooth muscle cells differentiate into lymphoid tissue organizer-like cells on combined tumor necrosis factor receptor-1/lymphotoxin β -receptor NF- κ B signaling. *Arterioscler. Thromb. Vasc. Biol* 30, 395–402. [PubMed: 20139367]
- Lutz ER, Wu AA, Bigelow E, Sharma R, Mo G, Soares K, Solt S, Dorman A, Wamwea A, Yager A, et al. (2014). Immunotherapy converts non-immunogenic pancreatic tumors into immunogenic foci of immune regulation. *Cancer Immunol. Res* 2, 616–631. [PubMed: 24942756]

- MacEwan DJ (2002). TNF receptor subtype signalling: differences and cellular consequences. *Cell. Signal* 14, 477–492. [PubMed: 11897488]
- Mahmoud SMA, Lee AHS, Paish EC, Macmillan RD, Ellis IO, and Green AR (2012). The prognostic significance of B lymphocytes in invasive carcinoma of the breast. *Breast Cancer Res. Treat* 132, 545–553. [PubMed: 21671016]
- Makowski D, Ben-Shachar MS, Patil I, and Lüdecke D (2020). Methods and Algorithms for Correlation Analysis in R. *J. Open Source Softw* 5, 2306.
- Maldonado L, Teague JE, Morrow MP, Jotova I, Wu TC, Wang C, Desmarais C, Boyer JD, Tycko B, Robins HS, et al. (2014). Intramuscular Therapeutic Vaccination Targeting HPV16 Induces T Cell Responses That Localize in Mucosal Lesions. *Sci. Transl. Med* 6, 221ra13.
- Mauldin IS, Sheybani ND, Young SJ, Price RJ, and Slingluff CL (2020). Deconvolution of the immunological contexture of mouse tumors with multiplexed immunohistochemistry. In *Methods in Enzymology*, Galluzzi L and Rudqvist N-P, eds. (Academic Press), pp. 81–93.
- McDonald KG, McDonough JS, and Newberry RD (2005). Adaptive immune responses are dispensable for isolated lymphoid follicle formation: antigen-naïve, lymphotoxin-sufficient B lymphocytes drive the formation of mature isolated lymphoid follicles. *J. Immunol* 174, 5720–5728. [PubMed: 15843574]
- Mebius RE (2003). Organogenesis of lymphoid tissues. *Nat. Rev. Immunol* 3, 292–303. [PubMed: 12669020]
- Medvedev AE, Espevik T, Ranges G, and Sundan A (1996). Distinct roles of the two tumor necrosis factor (TNF) receptors in modulating TNF and lymphotoxin alpha effects. *J. Biol. Chem* 271, 9778–9784. [PubMed: 8621658]
- Miller BC, Sen DR, Al Aboosy R, Bi K, Virkud YV, LaFleur MW, Yates KB, Lako A, Felt K, Naik GS, et al. (2019). Subsets of exhausted CD8⁺ T cells differentially mediate tumor control and respond to checkpoint blockade. *Nat. Immunol* 20, 326–336. [PubMed: 30778252]
- Motallebzadeh R, Rehakova S, Conlon TM, Win TS, Callaghan CJ, Goddard M, Bolton EM, Ruddle NH, Bradley JA, and Pettigrew GJ (2012). Blocking lymphotoxin signaling abrogates the development of ectopic lymphoid tissue within cardiac allografts and inhibits effector antibody responses. *FASEB J.* 26, 51–62. [PubMed: 21926237]
- Mueller CG, Nayar S, Campos J, and Barone F (2018). Molecular and Cellular Requirements for the Assembly of Tertiary Lymphoid Structures. *Adv. Exp. Med. Biol* 1060, 55–72. [PubMed: 30155622]
- Muniz LR, Pacer ME, Lira SA, and Furtado GC (2011). A critical role for dendritic cells in the formation of lymphatic vessels within tertiary lymphoid structures. *J. Immunol* 187, 828–834. [PubMed: 21666055]
- Nayar S, Campos J, Smith CG, Iannizzotto V, Gardner DH, Mourcin F, Roulois D, Turner J, Sylvestre M, Asam S, et al. (2019). Immunofibroblasts are pivotal drivers of tertiary lymphoid structure formation and local pathology. *Proc. Natl. Acad. Sci. USA* 116, 13490–13497. [PubMed: 31213547]
- Neyt K, Perros F, GeurtsvanKessel CH, Hammad H, and Lambrecht BN (2012). Tertiary lymphoid organs in infection and autoimmunity. *Trends Immunol.* 33, 297–305. [PubMed: 22622061]
- Onder L, and Ludewig B (2018). A Fresh View on Lymph Node Organogenesis. *Trends Immunol.* 39, 775–787. [PubMed: 30150089]
- Peduto L, Dulauroy S, Lochner M, Späth GF, Morales MA, Cumano A, and Eberl G (2009). Inflammation recapitulates the ontogeny of lymphoid stromal cells. *J. Immunol* 182, 5789–5799. [PubMed: 19380827]
- Perez-Ruiz E, Minute L, Otano I, Alvarez M, Ochoa MC, Belsue V, de Andrea C, Rodriguez-Ruiz ME, Perez-Gracia JL, Marquez-Rodas I, et al. (2019). Prophylactic TNF blockade uncouples efficacy and toxicity in dual CTLA-4 and PD-1 immunotherapy. *Nature* 569, 428–432. [PubMed: 31043740]
- Peschon JJ, Torrance DS, Stocking KL, Glaccum MB, Otten C, Willis CR, Charrier K, Morrissey PJ, Ware CB, and Mohler KM (1998). TNF receptor-deficient mice reveal divergent roles for p55 and p75 in several models of inflammation. *J. Immunol* 160, 943–952. [PubMed: 9551933]

- Peske JD, Thompson ED, Gemta L, Baylis RA, Fu Y-X, and Engelhard VH (2015). Effector lymphocyte-induced lymph node-like vasculature enables naive T-cell entry into tumours and enhanced anti-tumour immunity. *Nat. Commun* 6, 7114. [PubMed: 25968334]
- Peters A, Pitcher LA, Sullivan JM, Mitsdoerffer M, Acton SE, Franz B, Wucherpfennig K, Turley S, Carroll MC, Sobel RA, et al. (2011). Th17 cells induce ectopic lymphoid follicles in central nervous system tissue inflammation. *Immunity* 35, 986–996. [PubMed: 22177922]
- Petitprez F, de Reyniès A, Keung EZ, Chen TW-W, Sun C-M, Calderaro J, Jeng Y-M, Hsiao L-P, Lacroix L, Bougoüin A, et al. (2020). B cells are associated with survival and immunotherapy response in sarcoma. *Nature* 577, 556–560. [PubMed: 31942077]
- Pikor NB, Astarita JL, Summers-Deluca L, Galicia G, Qu J, Ward LA, Armstrong S, Dominguez CX, Malhotra D, Heiden B, et al. (2015). Integration of Th17- and lymphotoxin-derived signals initiates meningeal-resident stromal cell remodeling to propagate neuroinflammation. *Immunity* 43, 1160–1173. [PubMed: 26682987]
- Pula B, Witkiewicz W, Dziegiel P, and Podhorska-Okolow M (2013). Significance of podoplanin expression in cancer-associated fibroblasts: a comprehensive review. *Int. J. Oncol* 42, 1849–1857. [PubMed: 23588876]
- Rangel-Moreno J, Moyron-Quiroz JE, Hartson L, Kusser K, and Randall TD (2007). Pulmonary expression of CXC chemokine ligand 13, CC chemokine ligand 19, and CC chemokine ligand 21 is essential for local immunity to influenza. *Proc. Natl. Acad. Sci. USA* 104, 10577–10582. [PubMed: 17563386]
- Rangel-Moreno J, Carragher DM, de la Luz Garcia-Hernandez M, Hwang JY, Kusser K, Hartson L, Kolls JK, Khader SA, and Randall TD (2011). The development of inducible bronchus-associated lymphoid tissue depends on IL-17. *Nat. Immunol* 12, 639–646. [PubMed: 21666689]
- Reilly MJ, Morrow B, Ager CR, Liu A, Hong DS, and Curran MA (2019). TLR9 activation cooperates with T cell checkpoint blockade to regress poorly immunogenic melanoma. *J. Immunother. Cancer* 7, 323. [PubMed: 31771649]
- Rodriguez AB, and Engelhard VH (2020). Insights into tumor-associated tertiary lymphoid structures: novel targets for antitumor immunity and cancer immunotherapy. *Cancer Immunol. Res* 8, 1338–1345. [PubMed: 33139300]
- Rodriguez AB, Peske JD, and Engelhard VH (2018). Identification and characterization of tertiary lymphoid structures in murine melanoma. *Methods Mol. Biol* 1845, 241–257. [PubMed: 30141017]
- Ruddle NH, and Akirav EM (2009). Secondary lymphoid organs: responding to genetic and environmental cues in ontogeny and the immune response. *J. Immunol* 183, 2205–2212. [PubMed: 19661265]
- Rynne-Vidal A, Jiménez-Heffernan JA, Fernández-Chacón C, López-Cabrera M, and Sandoval P (2015). The Mesothelial Origin of Carcinoma Associated-Fibroblasts in Peritoneal Metastasis. *Cancers (Basel)* 7, 1994–2011. [PubMed: 26426054]
- Sato Y, Mii A, Hamazaki Y, Fujita H, Nakata H, Masuda K, Nishiyama S, Shibuya S, Haga H, Ogawa O, et al. (2016). Heterogeneous fibroblasts underlie age-dependent tertiary lymphoid tissues in the kidney. *JCI Insight* 1, e87680. [PubMed: 27699223]
- Sautès-Fridman C, Petitprez F, Calderaro J, and Fridman WH (2019). Tertiary lymphoid structures in the era of cancer immunotherapy. *Nat. Rev. Cancer* 19, 307–325. [PubMed: 31092904]
- Schrama D, thor Straten P, Fischer WH, McLellan AD, Bröcker EB, Reisfeld RA, and Becker JC (2001). Targeting of lymphotoxin- α to the tumor elicits an efficient immune response associated with induction of peripheral lymphoid-like tissue. *Immunity* 14, 111–121. [PubMed: 11239444]
- Stark FC, Weeratna RD, Deschatelets L, Gurnani K, Dudani R, McCluskie MJ, and Krishnan L (2017). An Archaeosome-Adjuvanted Vaccine and Checkpoint Inhibitor Therapy Combination Significantly Enhances Protection from Murine Melanoma. *Vaccines (Basel)* 5, 38.
- Thommen DS, Koelzer VH, Herzig P, Roller A, Trefny M, Dimeloe S, Kiialainen A, Hanhart J, Schill C, Hess C, et al. (2018). A transcriptionally and functionally distinct PD-1⁺ CD8⁺ T cell pool with predictive potential in non-small-cell lung cancer treated with PD-1 blockade. *Nat. Med* 24, 994–1004. [PubMed: 29892065]

- Thompson ED, Enriquez HL, Fu Y-X, and Engelhard VH (2010). Tumor masses support naive T cell infiltration, activation, and differentiation into effectors. *J. Exp. Med* 207, 1791–1804. [PubMed: 20660615]
- Trout AT, Rabinowitz RS, Platt JF, and Elsayes KM (2013). Melanoma metastases in the abdomen and pelvis: Frequency and patterns of spread. *World J. Radiol* 5, 25–32. [PubMed: 23494131]
- Turnquist HR, Lin X, Ashour AE, Hollingsworth MA, Singh RK, Talmadge JE, and Solheim JC (2007). CCL21 induces extensive intratumoral immune cell infiltration and specific anti-tumor cellular immunity. *Int. J. Oncol* 30, 631–639. [PubMed: 17273764]
- van de Pavert SA, and Mebius RE (2010). New insights into the development of lymphoid tissues. *Nat. Rev. Immunol* 10, 664–674. [PubMed: 20706277]
- Wajant H, and Siegmund D (2019). TNFR1 and TNFR2 in the Control of the Life and Death Balance of Macrophages. *Front. Cell Dev. Biol* 7, 91. [PubMed: 31192209]
- Wu Q, Wang Y, Wang J, Hedgeman EO, Browning JL, and Fu YX (1999). The requirement of membrane lymphotoxin for the presence of dendritic cells in lymphoid tissues. *J. Exp. Med* 190, 629–638. [PubMed: 10477548]
- Yu P, Lee Y, Liu W, Chin RK, Wang J, Wang Y, Schietinger A, Philip M, Schreiber H, and Fu YX (2004). Priming of naive T cells inside tumors leads to eradication of established tumors. *Nat. Immunol* 5, 141–149. [PubMed: 14704792]
- Yu P, Lee Y, Wang Y, Liu X, Auh S, Gajewski TF, Schreiber H, You Z, Kaynor C, Wang X, and Fu YX (2007). Targeting the primary tumor to generate CTL for the effective eradication of spontaneous metastases. *J. Immunol* 179, 1960–1968. [PubMed: 17641063]

Highlights

- Cancer-associated fibroblasts orchestrate tertiary lymphoid structures in tumors
- CD8 T cells and B cells drive tertiary lymphoid structure development via fibroblasts
- Tertiary lymphoid structure development is mediated by TNF and lymphotoxin receptors
- Checkpoint blockade alters tertiary lymphoid structures together with tumor control

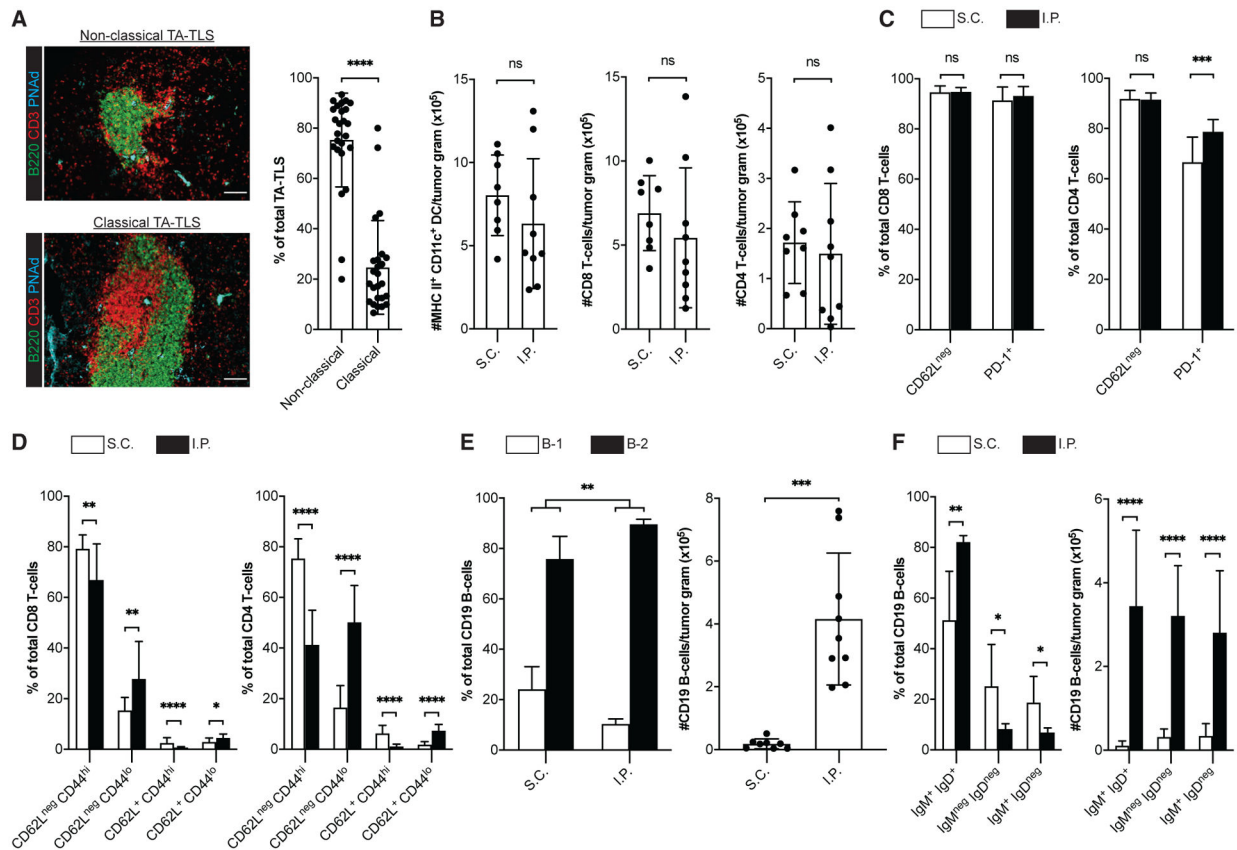


Figure 1. TA-TLSs in I.P. tumors are associated with enhanced representations of distinctly differentiated T cells and naive B cells

(A–F) Day 14 S.C. or I.P. B16-OVA tumors from C57BL/6 (WT) mice were prepared for IF (A) or flow cytometry (B–F) as described in STAR Methods. (A) Representative images and summary data for TA-TLS organizational types in I.P. tumors. Scale bar: 100 μ m. Data are from five experiments; $n = 25$ tumors. (B–F) CD45⁺ single-cell suspensions were stained with the indicated markers to define subpopulations (DC = CD3^{neg} CD19^{neg} CD11c⁺ MHC II⁺; T cells = CD19^{neg} CD3⁺ CD8⁺ or CD4⁺; B cells = CD3^{neg} CD19⁺ CD5⁺ or CD5^{neg}) and activation state and were quantitated by flow cytometry.

Data are from two to five experiments; $n = 8–18$ tumors per group. Results are mean \pm standard deviation (SD), analyzed by unpaired Welch's t test. ^{ns} $p > 0.05$, * $p < 0.05$, ** $p < 0.01$, *** $p < 0.001$, **** $p < 0.0001$.

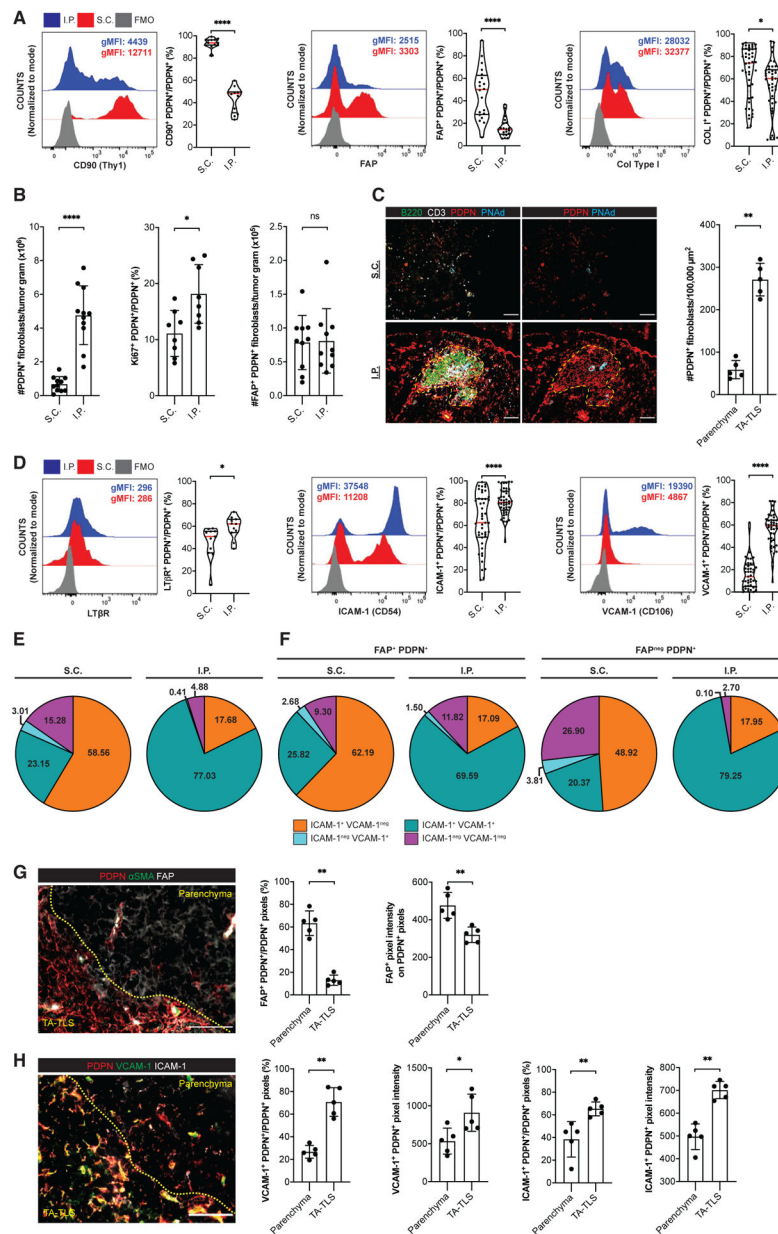


Figure 2. A population of CAF from I.P. tumors exhibit lymphoid tissue organizer cell characteristics

(A–E, G, and H) Day 14 S.C. or I.P. B16-OVA tumors from WT mice were prepared for flow cytometry (A, B, D, and E) or IF (C, G, and H) as described in STAR Methods. (A and D) Left, representative histograms and geometric mean fluorescence intensities (gMFIs) of indicated markers on PDPN^{hi} CD31^{neg} CD45^{neg} Ter119^{neg} CAF. gMFIs calculated on cells gated above the fluorescence minus one (FMO) control. Right, percentage of CAF expressing indicated markers. Data are from two to five experiments; n = 11–45 tumors per group.

(B, E, and F) CAF subpopulations were quantitated by flow cytometry. Data are from two to three experiments; n = 8–11 tumors per group.

(C, G, and H) Left, representative images of tumors stained with indicated markers. Yellow dashes delimit TA-TLS area. Scale bar: 100 μm . Right, summary data of PDPN⁺ CAF densities (C) and marker expression in parenchymal and TA-TLS regions (G and H) from one experiment; n = 5 tumors per group. Pixel intensities were calculated using a PDPN mask.

Results are mean \pm SD analyzed by unpaired Welch's t test. ^{ns}p > 0.05, **p < 0.01, ***p < 0.001, ****p < 0.0001.

Author Manuscript

Author Manuscript

Author Manuscript

Author Manuscript

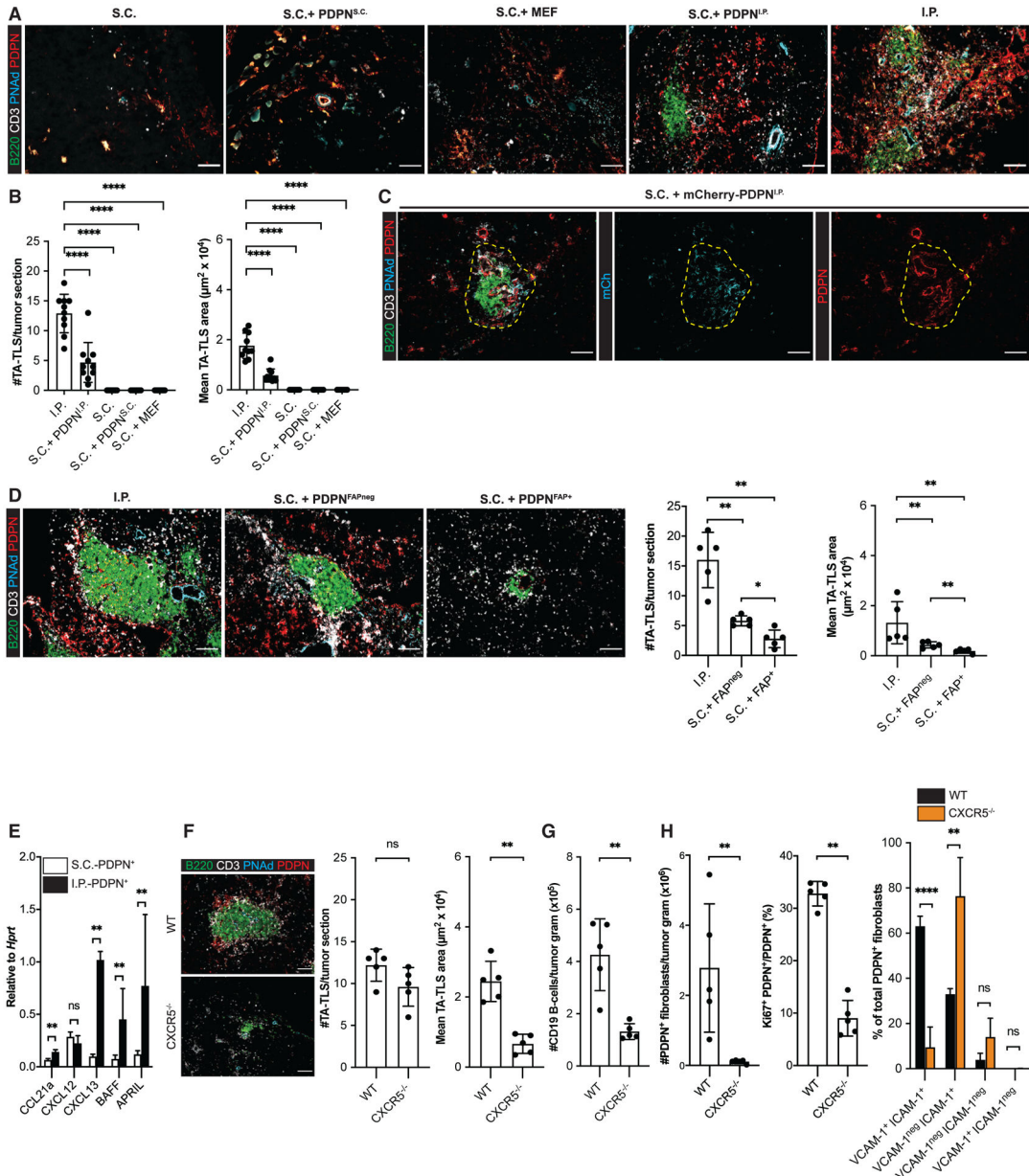


Figure 3. CAF act as surrogate lymphoid tissue organizer cells that orchestrate TA-TLS formation

(A–D) S.C. tumors were induced by co-injection of B16-OVA cells together with the indicated populations of fibroblasts. Day 14 S.C. or I.P. tumors were prepared for IF as described in STAR Methods. (A, C, and D, left) Representative images. Yellow dashed region (C) represents TA-TLS area. Scale bar: 100 μm. (B and D, right) Summary data from one to two experiments; n = 5 or 10 tumors per group.

(E) CAF from day 14 S.C. and I.P. tumors were purified, and expression of the indicated RNA transcripts was determined as described in STAR Methods. Data from two experiments presented as 2^{-CT} relative to *Hprt*, n = 6 tumors per group.

(F–H) Day 14 I.P. tumors from WT or CXCR5^{-/-} mice were prepared for IF (F) or flow cytometry (G and H) as described in STAR Methods. (F) Left: representative images. Scale

bar: 100 μm . Right: summary data from one experiment; $n = 5$ tumors per group. (G and H) Cell populations were quantitated as outlined in Figures 1 and 2. Data represent one experiment; $n = 5$ tumors per group.

Results are mean \pm SD, analyzed using Kruskal-Wallis H test with Dunn's post-test (B and D) or unpaired Welch's t test (E-H). ^{ns} $p > 0.05$, * $p < 0.05$, ** $p < 0.01$, **** $p < 0.0001$.

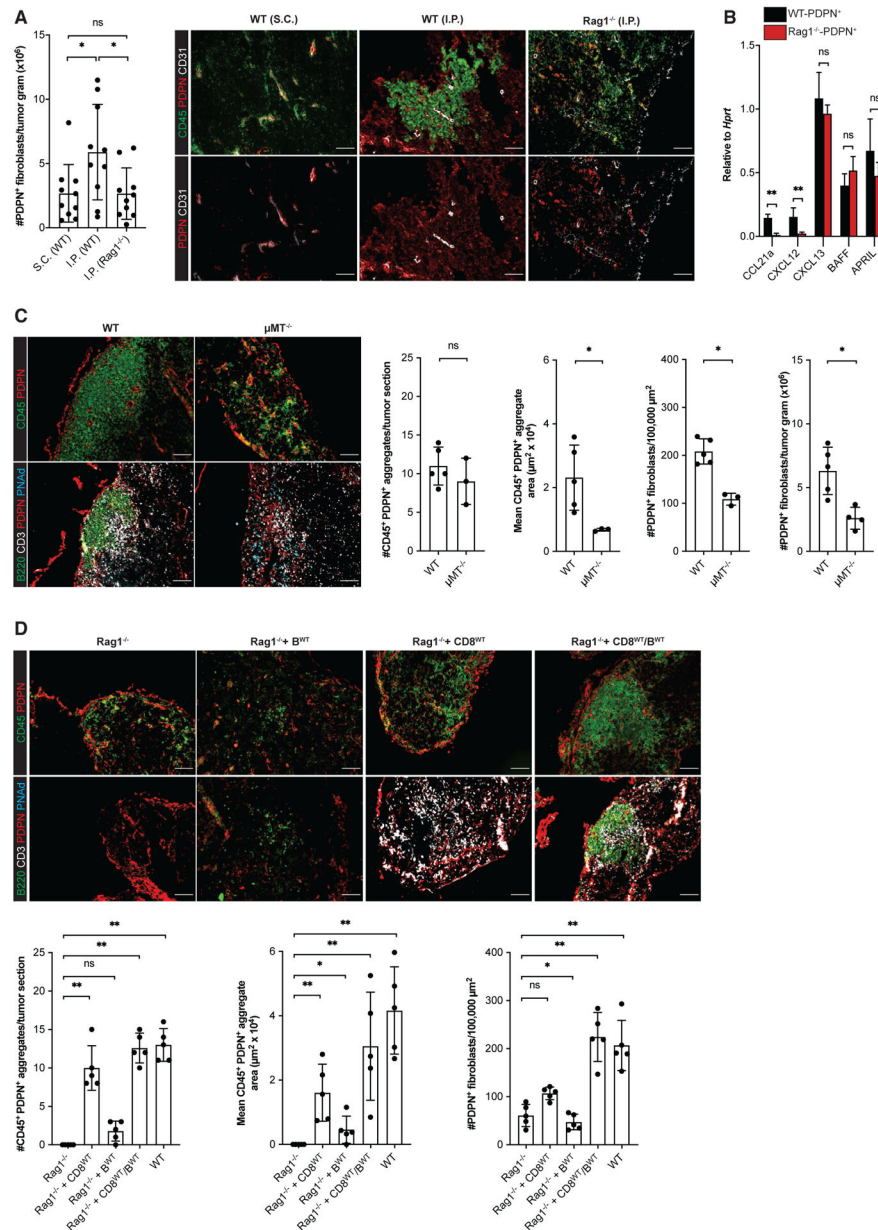


Figure 4. CD8 T cells and B cells act coordinately as lymphoid tissue inducer cells driving TA-TLS development

(A, C, and D) Day 14 I.P. B16-OVA tumors from WT mice, μ MT $^{-/-}$ mice, Rag1 $^{-/-}$ mice, and Rag1 $^{-/-}$ mice repleted with CD8 T cells and/or B cells 3 days prior to tumor implantation were prepared for and analyzed by flow cytometry or IF as described in STAR Methods. Scale bars: 100 μ m. Data are from one to two experiments; n = 3–10 tumors per group.

(B) CAF from day 14 i.p. tumors from WT or Rag1 $^{-/-}$ mice were purified, and expression of the indicated RNA transcripts was determined as described in STAR Methods. Data from two experiments presented as 2^{-CT} relative to *Hprt*; n = 6 tumors per group.

Results are mean \pm SD analyzed using Kruskal-Wallis H test with Dunn's post-test (A and D) or unpaired Welch's t test (B and C). ns $p > 0.05$, * $p < 0.05$, ** $p < 0.01$, **** $p < 0.0001$.

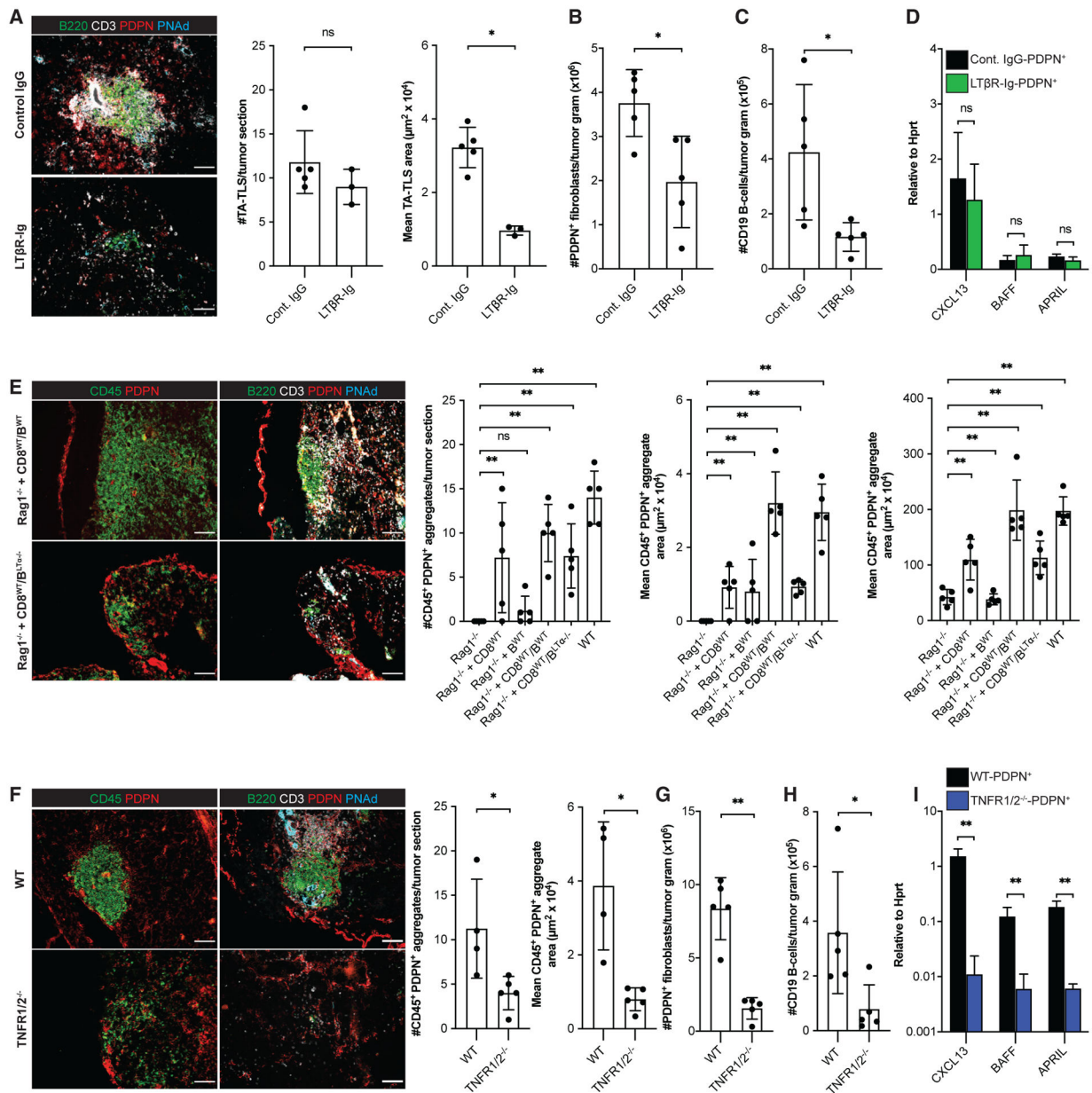


Figure 5. Induction and robust development of PDPN⁺ reticular networks in TA-TLS are regulated by TNFR and LTbR signaling, respectively

Day 14 I.P. B16-OVA tumors from WT mice, WT mice treated with LTβR-Ig fusion protein, TNFR1/2^{-/-} mice, Rag1^{-/-} mice, and Rag1^{-/-} mice repleted with CD8 T cells and/or B cells 3 days prior to tumor implantation were analyzed by IF or flow cytometry as described in STAR Methods. (A, E, and F) Scale bars: 100 μm. Data are from one experiment; n = 3–5 tumors per group.

(B, C, G, and H) Data are from one experiment; n = 5 tumors per group.

(D and I) CAF from day 14 i.p. tumors from WT mice, WT mice treated with LTβR-Ig, or TNFR1/2^{-/-} mice were purified and expression of the indicated RNA transcripts determined as described in STAR Methods. Data are from two experiments presented as 2^{-CT} relative to *Hprt*; n = 6 tumors per group.

Results are mean \pm SD analyzed using unpaired Welch's t test (A–D and F–I) or Kruskal-Wallis H test with Dunn's post-test (E). ^{ns}p > 0.05, *p < 0.05, **p < 0.01.

Author Manuscript

Author Manuscript

Author Manuscript

Author Manuscript

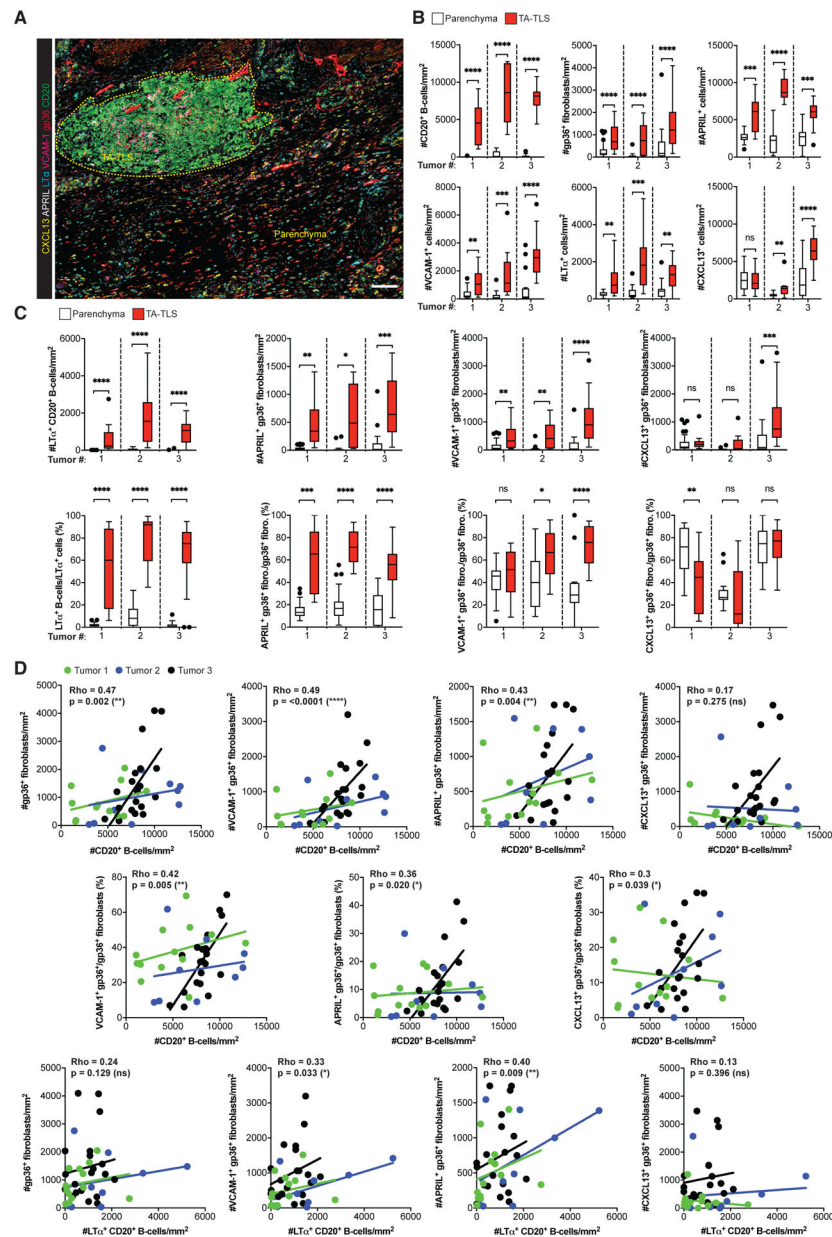


Figure 6. Human TA-TLS are associated with LT⁺ B cells and a co-extensive reticular network of CAF with lymphoid tissue organizer characteristics

Human melanoma biopsies containing TA-TLS were collected, prepared, stained, and analyzed as described in STAR Methods.

(A) Representative image of a TA-TLS-containing melanoma sample. Dashed yellow line represents TA-TLS area. Scale bar: 100 μ m.

(B and C) Densities and percentages of single- (B) and dual-stained (C) cell populations in parenchyma and TA-TLS regions of tumors from three patients ($n = 12$ –39 parenchyma and TA-TLS regions of interest). Data were analyzed by Wilcoxon rank-sum test, and boxplots were generated according to Tukey's method.

(D) Correlations between density of B cell populations and density or fraction of fibroblast populations. Dots represent individual TA-TLS. Each line represents the correlation for an

individual tumor. Rho represents the multilevel correlation coefficient for the three tumors. Spearman's linear mixed-models multilevel correlation analysis was determined for all tumors together to account for the nested data structure. ^{ns}p > 0.05, *p < 0.05, **p < 0.01, ***p < 0.001, ****p < 0.0001.

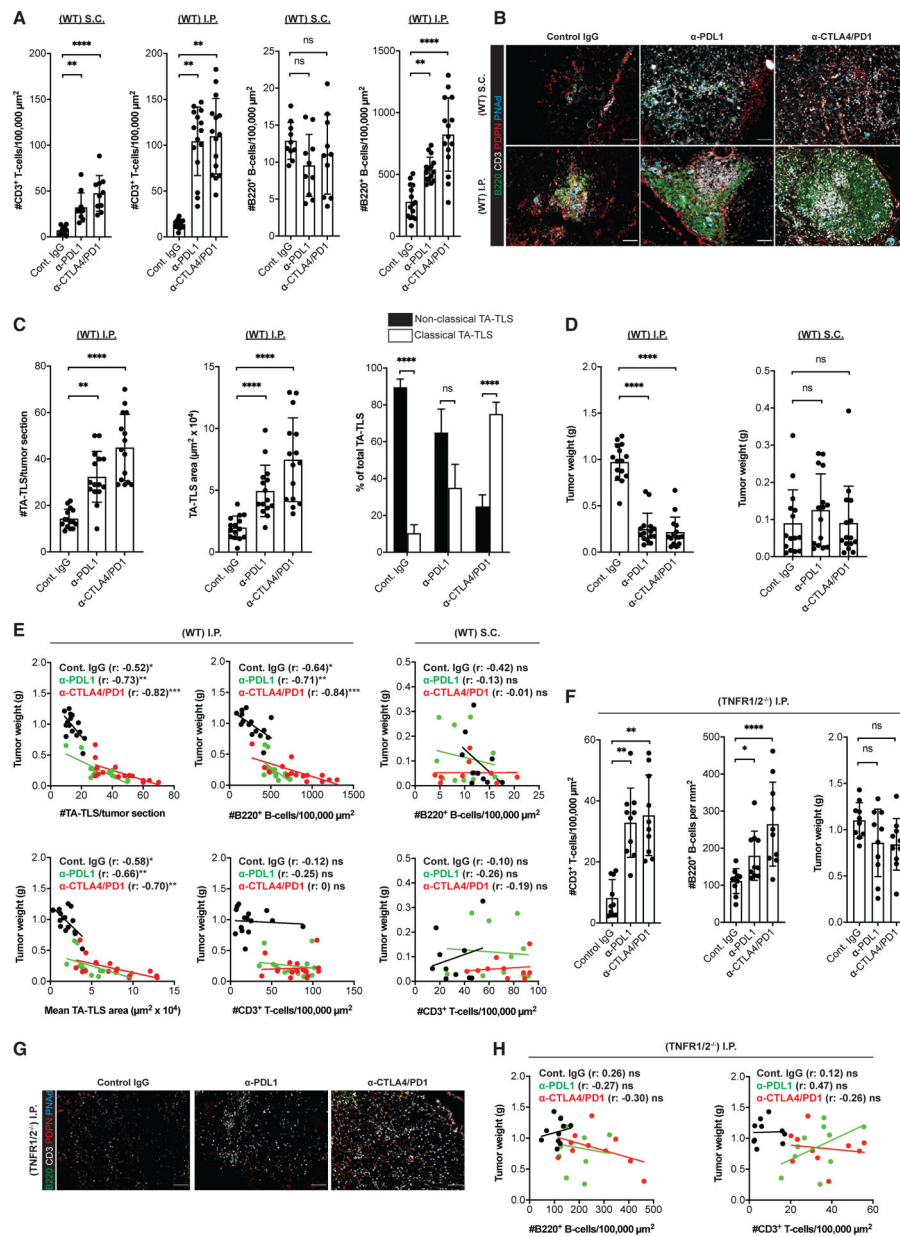


Figure 7. TA-TLS number, size, and organization are augmented by checkpoint immunotherapy and correlated with tumor control

WT or TNFR1/2^{-/-} mice were treated with control IgG, anti-PDL1, or anti-CTLA4/PD1 beginning 3 days after S.C. or I.P. tumor implantation. Tumors were harvested on day 14, weighed, and prepared for IF.

(A) Summary data for intratumoral parenchymal (non-TA-TLS) T and B cell densities in WT mouse tumors.

(B) Representative images showing typical TA-TLS size and organization in tumors from WT mice treated as indicated. Scale bar: 100 μm .

(C) Summary data of TA-TLS characteristics in tumors from WT mice. Classical TA-TLS are distinguished from non-classical by the presence of distinct T and B cell compartments.

(D) Tumor weights determined at harvest on day 14.

(E) Spearman correlation analysis of WT mouse tumor weights with TA-TLS number, size, or densities of intratumoral parenchymal T and B cells. Each dot represents an individual tumor.

(F) Left and middle: summary data for intratumoral parenchymal (non-TA-TLS) T and B cell densities in TNFR1/2^{-/-} mouse tumors. Right: tumor weights were determined at harvest on day 14.

(G) Representative intratumoral images of i.p. tumors from TNFR1/2^{-/-} mice treated as indicated. Scale bars: 100 μ m.

(H) Spearman correlation analysis of TNFR1/2^{-/-} mouse tumor weights with densities of T and B cells. Each dot represents an individual tumor.

(A–E) Data are from two to three experiments; n = 10–15 tumors per group. (F–H) Data are from two experiments; n = 10 tumors per group. Results shown as mean \pm SD analyzed using Kruskal-Wallis H test with Dunn's post-test (A, C, D, and F) or Spearman's multilevel correlation analysis (E and H). ^{ns}p > 0.05, *p < 0.05, **p < 0.01.

KEY RESOURCES TABLE

REAGENT or RESOURCE	SOURCE	IDENTIFIER
Antibodies		
eFluor 450 anti-mouse CD4	ThermoFisher Scientific	Catalog #: 48-0042-82; Clone:RM4-5; RRID:AB_1272194
Brilliant Violet 605 anti-mouse PD1	Biolegend	Catalog #: 135220; Clone: 29F.1A12; RRID:AB_2562616
Brilliant Violet 650 anti-mouse CD62L	Biolegend	Catalog #: 104453; Clone: MEL-14; RRID:AB_2800559
Brilliant Violet 785 anti-mouse CD45	Biolegend	Catalog #: 103149; Clone: 30-F11; RRID:AB_2564590
FITC anti-mouse TIM-3	ThermoFisher Scientific	Catalog #: 11-5870-82; Clone: RMT3-23; RRID:AB_2688129
PerCP-eFluor 710 anti-mouse CD8 alpha	ThermoFisher Scientific	Catalog #: 46-0081-82; Clone: 53-6.7; RRID:AB_1834433
PE anti-mouse LAG-3	Biolegend	Catalog #: 125208; Clone: C9B7W; RRID:AB_2133343
PE/Dazzle 594 anti-mouse CD44	Biolegend	Catalog #: 103056; Clone: IM7; RRID:AB_2564044
PE-Cy7 anti-mouse Ki67	ThermoFisher Scientific	Catalog #: 25-5698-82; Clone: SolA15; RRID:AB_11220070
Alexa Fluor 647 anti-mouse CD3	Biolegend	Catalog #: 100209; Clone: 17A2; RRID:AB_389323
APC-Cy7 anti-mouse CD19	Biolegend	Catalog #: 115530; Clone: 6D5; RRID:AB_830707
eFluor 450 anti-mouse IgM	ThermoFisher Scientific	Catalog #: 48-5890-82; Clone: eB121-15F9; RRID:AB_10671539
PE/Dazzle 594 anti-mouse IgD	Biolegend	Catalog #: 405742; Clone: 11-26c.2a; RRID:AB_2571985
PerCP-Cy5.5 anti-mouse CD11c	Biolegend	Catalog #: 117328; Clone: N418; RRID:AB_2129641
PE anti-mouse I-A/I-E (MHC II)	Biolegend	Catalog #: 107608; Clone: M5/114.15.2; RRID:AB_313323
Pacific Blue anti-mouse ICAM-1 (CD54)	Biolegend	Catalog #: 116116; Clone: YN1/1.7.4; RRID:AB_2121771
Brilliant Violet 605 anti-mouse VCAM-1 (CD106)	BD Bioscience	Catalog #: 745193; Clone: 429; RRID:AB_2742789
Alexa Fluor 488 polyclonal Collagen Type I	SoutherBiotech	Catalog #: 1310-30; Clone: Poly; RRID:AB_2794728
PerCP-eFluor 710 anti-mouse CD31	ThermoFisher Scientific	Catalog #: 46-0311-82; Clone: 390; RRID:AB_1834429
Unconjugated anti-mouse alpha smooth muscle actin	ThermoFisher Scientific	Catalog #: 14-9760-82; Clone: 1A4; RRID:AB_2572996
PE anti-mouse IgG2a	Biolegend	Catalog #: 407108; Clone: RMG2a-62; RRID:AB_10549456
PE/Dazzle 594 anti-mouse CD140 alpha	Biolegend	Catalog #: 135922; Clone: APA5; RRID:AB_2814035
PE-Cy7 anti-mouse podoplanin (gp38)	Biolegend	Catalog #: 127412; Clone: 8.1.1; RRID:AB_10613648
eFluor 660 anti-mouse Ki67	ThermoFisher Scientific	Catalog #: 50-5698-82; Clone: SolA15; RRID:AB_2574235
Unconjugated anti-mouse FAP	Millipore Sigma	Catalog #: MABC1145; Clone: 73.3; RRID:AB_2892562

REAGENT or RESOURCE	SOURCE	IDENTIFIER
APC-Cy7 anti-mouse IgG1	Biolegend	Catalog #: 406620; Clone: RMG1-1; RRID:AB_2571947
PE/Dazzle 594 anti-mouse PD-L1	Biolegend	Catalog #: 124324; Clone: 10F.9G2; RRID:AB_2565639
APC anti-mouse CD120 alpha (TNF R Type I/p55)	Biolegend	Catalog #: 113006; Clone: 55R-286; RRID:AB_2208779
Brilliant Violet 421 anti-mouse CD120 beta (TNF R Type II/p75)	BD Bioscience	Catalog #: 564088; Clone: TR75-89; RRID:AB_2738585
PE/Dazzle 594 anti-mouse CD90.2 (Thy-1.2)	Biolegend	Catalog #: 140329; Clone: 53-2.1; RRID:AB_2650965
APC anti-mouse lymphotoxin beta receptor (LTβR)	Biolegend	Catalog #: 134408; Clone: 5G11; RRID:AB_2728151
DyLight 550 Anti-Mouse/Human CD45R (B220)	Leinco Technologies (Discontinued)	Catalog #: C1944; Clone: RA3-6B2; RRID:AB_2829026
Unconjugated anti-mouse Podoplanin (gp38)	Biolegend	Catalog #: 127402; Clone: 8.1.1; RRID:AB_1089187
Biotin anti-mouse/human PNAd	Biolegend	Catalog #: 120804; Clone: MECA-79; RRID:AB_493557
Alexa Fluor 488 anti-mouse CD45	Biolegend	Catalog #: 103122; Clone: 30-F11; RRID:AB_493531
Biotin anti-mouse ICAM-1 (CD54)	Biolegend	Catalog #: 116103; Clone: YN1/1.7.4; RRID:AB_313694
Alexa Fluor 647 anti-mouse VCAM-1 (CD106)	Biolegend	Catalog #: 105712; Clone: 429; RRID:AB_493429
Alexa Fluor 488 AffiniPure Goat Anti-Syrian Hamster IgG (H+L)	Jackson Labs	Catalog #: 107-545-142; Clone: Poly; RRID:AB_2337478
Rhodamine (TRITC) AffiniPure Goat Anti-Syrian Hamster IgG (H+L)	Jackson Labs	Catalog #: 107-025-142; Clone: Poly; RRID:AB_2337452
Rhodamine (TRITC) AffiniPure Donkey Anti-Mouse IgG (H+L)	Jackson Labs	Catalog #: 715-025-150; Clone: Poly; RRID:AB_2340766
Alexa Fluor 350 Streptavidin	ThermoFisher Scientific	Catalog #: S11249; Clone: N/A
<i>In Vivo</i> Plus anti-mouse PD-L1 (B7-H1)	BioXcell	Catalog #: BP0101; Clone: 10F.9G2; RRID:AB_10949073
<i>In Vivo</i> Plus anti-mouse PD-1 (CD279)	BioXcell	Catalog #: BP0273; Clone: 29F.1A12; RRID:AB_2687796
<i>In Vivo</i> Plus anti-mouse CTLA-4 (CD152)	BioXcell	Catalog #: BP0032; Clone: UC10-4F10-11; RRID:AB_1107598
Biotin anti-mouse Podoplanin	Biolegend	Catalog #: 127404; Clone: 8.1.1; RRID:AB_1134222
Biotin anti-mouse CD31	Biolegend	Catalog #: 102404; Clone: 390; RRID:AB_312899
CD45 MicroBeads, mouse	Miltenyi Biotec	Catalog #: 130-097-153
Anti-Biotin MicroBeads	Miltenyi Biotec	Catalog #: 130-097-046
<i>In Vivo</i> Ab anti-mouse CD16/CD32	BioXcell	Catalog #: BE0307; Clone: 2.4G2; RRID:AB_2736987
Unconjugated anti-mouse/human Lymphotoxin alpha (LTA)	Abcam	Catalog #: ab100844; Clone: AT15A3; RRID:AB_10672573
Unconjugated anti-human VCAM-1	Nordic Biosite	Catalog #: LS-C391116-20; Clone: 1.4C3; RRID:AB_2892563
Unconjugated anti-human CXCL13	Novus Biological	Catalog #: NBP2-16041; Clone: Poly; RRID:AB_2892564
Unconjugated anti-human/Rat/Mouse APRIL	Abcam	Catalog #: ab200836; Clone: EPR14588; RRID:AB_2892565

REAGENT or RESOURCE	SOURCE	IDENTIFIER
Unconjugated anti-human gp36	Abcam	Catalog #: ab236529; Clone: EPR22182; RRID:AB_2889051
Unconjugated anti-human CD20	Agilent	Catalog #: M075501-2; Clone: L26; RRID:AB_2892566
Unconjugated anti-mouse CD4	Abcam	Catalog #: ab183685; Clone: EPR19514; RRID:AB_2686917
Unconjugated anti-mouse CD8	Abcam	Catalog #: ab237723; Clone: CAL38; RRID:AB_2864723
Unconjugated anti-mouse CD19	Cell Signaling Technology	Catalog #: 90176S; Clone: D4V4B; RRID:AB_2800152
Unconjugated anti-human/rat/mouse CD34	Abcam	Catalog #: ab81289; Clone: EP373Y; RRID:AB_1640331
Unconjugated anti-mouse CD11c	Abcam	Catalog #: ab219799; Clone: EPR21826; RRID:AB_2864725
Biological samples		
Melanoma tissue samples from patients	This paper	N/A
Chemicals, peptides, and recombinant proteins		
Recombinant LT β R-Ig fusion protein	Wu et al. (1999) J. Exp. Med. 190, 629	N/A
DNase I	Sigma	Catalog #: 11284932001
Collagenase/Dispase	Sigma	Catalog #: 11097113001
Collagenase P	Sigma	Catalog #: 11213865001
Red Blood Cell Lysing Buffer Hybri-Max	Sigma	Catalog #: R7757-100ML
LIVE/DEAD Fixable Aqua Dead Cell Stain Kit	ThermoFisher Scientific	Catalog #: L34966
4',6-Diamidino-2'-phenylindole dihydrochloride (DAPI)	Sigma	Catalog #: 10236276001
Ethylenediaminetetraacetic acid (EDTA)	Sigma	Catalog #: EDS-1KG
Sodium azide	Sigma	Catalog #: S2002-500G
Methanol	Sigma	Catalog #: 34860-1L-R
Formalin solution, neutral buffered, 10%	Sigma	Catalog #: HT501128-4L
ProLong Gold Antifade Mountant with DAPI	ThermoFisher Scientific	Catalog #: P36931
ProLong Gold Antifade Mountant	ThermoFisher Scientific	Catalog #: P36930
Critical commercial assays		
Fixation/Permeabilization Solution Kit	BD Bioscience	Catalog #: 554714
Transcription Factor Buffer Set	BD Bioscience	Catalog #: 562574
RNAsprotect Cell Reagent	QIAGEN	Catalog #: 76526
RPMI 1640 Medium (Mod.) 1X with L-Glutamine	Fisher Scientific	Catalog #: MT-10043CV
DMEM with L-Glutamine, 4.5g/L Glucose and Sodium Pyruvate	Fisher Scientific	Catalog #: MT10013CV
IMDM, GlutaMAX	ThermoFisher Scientific	Catalog #: 31980030
L-Glutamine (200 mM)	ThermoFisher Scientific	Catalog #: 25030081
HEPES (1 M)	ThermoFisher Scientific	Catalog #: 15630080
CD8a T Cell Isolation Kit, mouse	Miltenyi Biotec	Catalog #: 130-104-075
B Cell Isolation Kit, mouse	Miltenyi Biotec	Catalog #: 130-090-862
Biotin Tyramide signal amplification	PerkinElmer	Catalog #: NEL700001KT
Avidin/Biotin Blocking Kit	Vector Laboratories	Catalog #: SP-2001

REAGENT or RESOURCE	SOURCE	IDENTIFIER
Opal 7-Color IHC Kits	Akoya Biosciences	Catalog #: NEL811001KT
AR9 Antigen Retrieval Buffer	Akoya Biosciences	Catalog #: AR9001KT
RNeasy Micro Kit	QIAGEN	Catalog #: 74004
RNeasy Mini Kit	QIAGEN	Catalog #: 74104
High-Capacity cDNA Reverse Transcription Kit	ThermoFisher Scientific	Catalog #: 4368814
TaqMan Fast Advanced Master Mix	ThermoFisher Scientific	Catalog #: 4444557
Experimental models: Cell lines		
B16-OVA	Hargadon et al. (2006) J. Immunol. 177, 6081	N/A
MC38-OVA	Hargadon et al. (2006) J. Immunol. 177, 6081	N/A
LLC-OVA	Gift of E. Podack (Univ of Miami)	N/A
Experimental models: Organisms/strains		
C57BL/6	Charles River/NCI	Catalog #: 027
Rag1 ^{-/-}	Jackson Labs	Catalog #: 002216
μMT ^{-/-}	Jackson Labs	Catalog #: 002288
LTa ^{-/-}	Jackson Labs	Catalog #: 002258
TNFR1/2 ^{-/-}	Jackson Labs	Catalog #: 003243
Human ubiquitin C Promoter (UBC)-mCherry	Jackson Labs	Catalog #: 017614
CXCR5 ^{-/-}	Jackson Labs	Catalog #: 006659
Rag2 ^{-/-} Il2rg ^{-/-}	Taconic Labs	Catalog #: 4111-F
Oligonucleotides		
CCL21a	ThermoFisher Scientific	Assay ID: Mm03646971_gH
CXCL12	ThermoFisher Scientific	Assay ID: Mm00445552_m1
CXCL13	ThermoFisher Scientific	Assay ID: Mm00444533_m1
TNFSF13 (APRIL)	ThermoFisher Scientific	Assay ID: Mm03809849_s1
TNFSF13b (BAFF)	ThermoFisher Scientific	Assay ID: Mm01218923_g1
Software and algorithms		
FlowJo v10.7 software	BD Bioscience	https://www.flowjo.com/
ImageJ software	NIH	https://imagej.nih.gov/ij/
Imaris image analysis software	Bitplane	https://imaris.oxinst.com/
Photoshop 2021	Adobe	https://www.adobe.com/
Vectra 3 Automated Quantitative Pathology Imaging System	Akoya Biosciences	https://www.akoyabio.com/
Phenochart Whole Slide Viewer	Akoya Biosciences	https://www.akoyabio.com/
InForm Tissue Analysis Software	Akoya Biosciences	https://www.akoyabio.com/
HALO Image Analysis Platform Software	IndicaLabs	https://indicalab.com/halo/
QuantStudio 6 Flex Real-Time PCR system	Applied Biosystem	https://www.thermofisher.com/us/en/home/life-science/pcr/real-time-pcr/real-time-pcr-instruments/quantstudio-systems/models/quantstudio-6-7-flex.html
R version 4	R Studios	https://www.r-project.org/
Prism version 7.0	GraphPad	https://www.graphpad.com/

REAGENT or RESOURCE	SOURCE	IDENTIFIER
SAS software suite version 9.4	SAS	https://www.sas.com/en_us/home.html

Author Manuscript

Author Manuscript

Author Manuscript

Author Manuscript